Politecnico di Torino

DEPARTMENT OF ELECTRONICS AND TELECOMMUNICATIONS

Master's Degree in Electronic Engineering

A.a. 2025/2026

Graduation Session March 2026

Metaprisms for Smart Radio Environments

Supervisors:
Giuseppe Vecchi
Paola Pirinoli

Author:
Valerio Di Tella

There is no prize to perfection,
only an end to pursuit
– Viktor (Arcane)

Acknowledgements

Vorrei prendere questa occasione per ringraziare tutti coloro che mi hanno permesso di raggiungere questo obiettivo.
Volevo quindi ringraziare i professori che mi hanno seguito, il professor Giuseppe Vecchi e la professoressa Paola Pirinoli per il loro aiuto e il loro costante supporto attraverso questo percorso di tesi.
Vorrei poi dedicare questa tesi alla mia famiglia, mia madre Flora, mio padre Costantino e mio fratello Giacomo, pilastri fondamentali della mia vita per esserci sempre stati e per avermi sempre appoggiato e sostenuto in ogni decisione della mia vita. Grazie per aver creduto in me con una naturalezza che mi ha insegnato cosa significhi davvero sentirsi sostenuti.
Alla mia ragazza, Chiara, con cui ho condiviso ogni passo di questo percorso, e in ogni momento mi ha fatto sentire amato e all'altezza delle sfide che affrontavo. Dedico questa tesi anche a te, che sei stata una fonte costante di forza e di felicità, sempre presente nei miei pensieri.
Vorrei poi ringraziare tutti i miei amici, che hanno accompagnato questo percorso dentro e fuori dallo studio, con voi ho condiviso tanti momenti importanti della mia vita. Grazie per esserci sempre stati per me.

Abstract

The increasing demand for high-data-rate wireless communications at millimeter-wave frequencies has highlighted the limitations of conventional propagation environments, where severe path loss and sensitivity to blockage degrade link reliability. In this context, the paradigm of Smart Radio Environments promotes the use of engineered electromagnetic surfaces to intentionally control wave propagation. Among the proposed implementations, reflective phase-gradient metasurfaces can operate as metaprisms, artificial structures that emulate the angular deflection mechanism of conventional optical prisms through engineered spatial phase distributions, enabling anomalous reflection and beam steering without mechanical reconfiguration. While theoretical models describe ideal continuous phase profiles, practical realizations rely on discretized unit cells constrained by geometry, dispersion, and bandwidth limitations, making the transition from theory to implementation a central challenge.

This thesis investigates a passive implementation strategy for reflective metaprisms based on a metallic smart skin operating around 28 GHz. The unit cell consists of a square waveguide aperture embedded in a perfectly electrically conducting slab, exploiting the dispersive behavior of waveguide propagation near the cutoff frequency of the dominant mode. In this regime, the reflected phase strongly depends on the electrical length of the guide, enabling phase control through variation of the waveguide length.

A systematic numerical investigation maps the relationship between waveguide length, reflection phase, and frequency, identifying a usable phase tuning range around the design frequency. This characterization forms the basis for the synthesis of finite metasurface configurations designed to operate as reflective metaprisms. The complete smart skin layout is modeled and simulated in CST Microwave Studio to evaluate beam steering capability, angular selectivity, and reflection efficiency. The results highlight the impact of discretization and dispersion on steering accuracy and bandwidth. Despite deviations from the ideal continuous model, the proposed design demonstrates stable and controllable anomalous reflection within the operational band.

The study demonstrates that a passive metaprism-based smart skin represents a viable low-complexity alternative to active reconfigurable intelligent

surfaces in scenarios requiring fixed beam steering, enabling path loss mitigation and improved link reliability. It therefore contributes to bridging theoretical phase-gradient concepts with physically implementable passive metasurface architectures for future millimeter-wave Smart Radio Environments.

Contents

List of Tables

List of Figures

Chapter 1

Introduction

1.1 Smart Radio Environments

Wireless connectivity has become a fundamental pillar of modern society, with emerging applications imposing unprecedented requirements in terms of data rate, latency, reliability, and energy efficiency. The migration toward millimeter-wave (mmWave) frequency bands in sixth-generation (6G) systems enables access to large spectral resources, but simultaneously introduces severe propagation challenges, including high free-space path loss, strong sensitivity to blockage, limited diffraction capability, and reduced penetration through common materials.

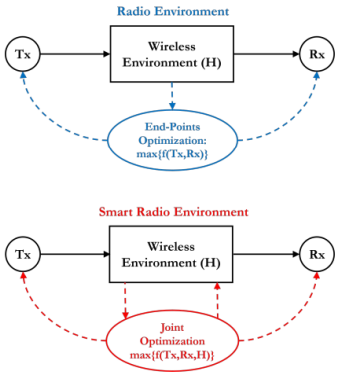

Figure 1.1: Functional principle of a Smart Radio Environments [1]

These intrinsic physical constraints significantly limit the robustness of conventional communication strategies. Traditional approaches rely on adapting transmitters and receivers through advanced beamforming, massive MIMO, or network densification. However, at mmWave frequencies, the propagation medium itself becomes a dominant performance-limiting factor, particularly in complex indoor and urban scenarios.

Figure 1.2: Examples of Implementation for Smart Radio Environments [1]

To address these challenges, next-generation wireless systems are envisioned to adopt a new architectural paradigm in which communication, sensing, localization, and computing functionalities are jointly supported [2]. Within this framework, the concept of Smart Radio Environments (SREs) has emerged as a promising strategy to overcome the physical limitations of high-frequency propagation [1]. The fundamental idea underlying SREs is to transform the wireless environment from a passive propagation medium into an engineered electromagnetic system capable of deliberately shaping wave propagation. Instead of exclusively optimizing transmitters and receivers, SREs introduce the possibility of controlling how electromagnetic waves interact with surrounding surfaces.
From an electromagnetic standpoint, Smart Radio Environments rely on the intentional engineering of boundary conditions [3]. By tailoring the local reflection, transmission, or absorption coefficients of distributed surfaces, it becomes possible to manipulate the amplitude, phase, and polarization of

impinging waves in a deterministic manner. In this sense, SREs extend the design space of wireless systems from active radiating devices to the physical environment itself.

This perspective shifts the role of walls, ceilings, and structural elements from passive scatterers to functional electromagnetic interfaces. By imposing spatially varying reflection properties across such interfaces, it is possible to redirect energy toward desired directions, enhance coverage in non-line-of-sight (NLoS) conditions, and mitigate destructive interference phenomena. Importantly, the SRE paradigm does not necessarily require active signal regeneration or amplification. Instead, it can be implemented through engineered surfaces that exploit controlled wave–matter interaction mechanisms. These surfaces modify the scattered field through passive or reconfigurable electromagnetic responses, enabling programmable manipulation of the propagation channel without conventional radio-frequency front-end architectures.

In this context, engineered electromagnetic surfaces constitute the physical layer upon which Smart Electromagnetic Skins are built. They provide the hardware platform that enables localized control of wave interaction, thereby bridging the gap between system-level communication objectives and electromagnetic wave engineering.

1.2 Smart Electromagnetic Skins

Smart Electromagnetic Skins (SESs), commonly referred to as smart skins, represent a broad class of engineered electromagnetic surfaces designed to intentionally control the propagation of incident waves through a prescribed spatial response. While metasurfaces provide the fundamental physical platform for wave manipulation, the smart skin concept emphasizes their functional role within engineered electromagnetic environments.

From a physical standpoint, a smart skin can be defined as a planar or conformal arrangement of sub-wavelength scattering elements whose collective electromagnetic behavior enables controlled reflection, transmission, or absorption of incident fields. The control mechanism can rely purely on geometrical design or it can incorporate tunable active components, depending on the intended application. In many implementations, this collective behavior can be described through an equivalent spatial distribution of surface reflection coefficients, effectively modifying the boundary conditions experienced by the incident field.

Smart skins can be classified into three main categories:

- Passive smart skins, whose electromagnetic response is entirely determined by their geometry, topology, and material composition. Once fabricated their functionality is fixed, and no external biasing or control circuitry is required;

- Reconfigurable smart skins, in which active tunable elements (e.g., varactors, PIN diodes, MEMS, or other components) enable dynamic adaptation of the local reflection or transmission coefficients depending on its use;

- Dispersive smart skins, which exploit the intrinsic frequency-dependent behavior of their unit cells to achieve frequency-selective wave manipulation without requiring active control.

It is important to distinguish the smart skin concept from Reconfigurable Intelligent Surfaces (RISs). RIS-based architectures represent a specific subclass of reconfigurable smart skins in which external electronic control allows real-time programmability of the surface response [1, 4]. However, the smart skin framework is more general and encompasses both passive and reconfigurable implementations.

Within the Smart Radio Environment paradigm, smart skins constitute the physical layer that transforms conventional propagation boundaries into engineered electromagnetic interfaces. By imposing a spatially varying reflection phase profile across the surface, passive smart skins can emulate functionalities traditionally achieved through bulky reflectors or phased arrays, but in an electrically thin and low-profile form factor.

Among the various possible implementations, reflective passive smart skins are particularly attractive for practical deployment due to their structural simplicity, low power consumption, low cost and ease of integration into existing infrastructures. In this configuration, the desired wavefront manipulation is achieved through the static design of the unit cells, that collectively impose a predetermined phase distribution across the structure.

This principle of operation leads to the concept of engineered reflective phase-gradient surfaces, working on redirecting the incident wave towards a prescribed direction thanks to a tailored spatial phase profile. A specific realization of this approach is the metaprism, which can be interpreted as a passive smart electromagnetic skin designed to emulate the functionality of a prism through spatial phase engineering. In this implementation, the spatial phase gradient is statically engineered during the design stage, allowing deterministic beam redirection without active control circuitry. This passive implementation is particularly attractive at mmWave frequencies, where losses and fabrication complexity become critical design constraints.

1.3 Metaprisms

A metaprism can be defined as a reflective phase-gradient surface intentionally engineered to exhibit a dispersive reflection response across its operating bandwidth. Unlike conventional metasurfaces designed to impose a fixed phase distribution at a single frequency, a metaprism leverages the intrinsic frequency-dependent behavior of its unit cells to produce a reflection phase profile that varies with frequency.
The metaprism concept was formally introduced in [5] in the context of wireless communications, where frequency dispersion is exploited to enable spatial manipulation of broadband signals. From an electromagnetic standpoint, however, the operation of a metaprism can be interpreted more generally as a consequence of engineered dispersive boundary conditions imposed by a reflective smart electromagnetic skin.
Because the reflection phase of each unit cell varies with frequency, the overall spatial phase profile generated across the surface becomes entangled with the frequency. As a result, different spectral components of an incident broadband signal experience different effective phase gradients. This phase gradient determines the direction of the reflected wavefront and enables spatial separation or redirection of energy across the signal bandwidth.
This behavior is consistent with the generalized Snell's law framework for phase-gradient metasurfaces [6], according to which the reflection angle is governed by the spatial derivative of the imposed phase discontinuity. In the case of metaprisms, the dispersive nature of the unit cells causes this phase gradient to vary with frequency, leading to frequency-dependent beam steering without requiring active tuning or real-time reconfiguration.
From a conceptual perspective, metaprisms can also be related to frequency-

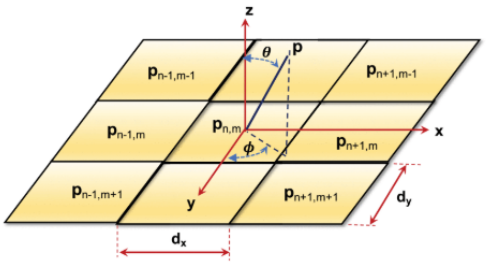

Figure 1.3: Basic structure of a metaprism [5]

selective surfaces (FSS), which have long been employed in microwave and optical systems for filtering, shielding, and radome applications [7]. While conventional FSS designs primarily exploit frequency selectivity to control transmission or reflection magnitude, metaprisms extend this concept by using dispersion to engineer the spatial distribution of the reflected field. In this sense, a metaprism may be regarded as an evolution of FSS-based structures toward controlled wavefront shaping.

From a system-level viewpoint, metaprisms represent an alternative paradigm to conventional reconfigurable intelligent surfaces. Their main advantages can be summarized as follows:

- they are fully passive structures and therefore do not require external power supply or biasing networks;
- their electromagnetic response is inherently defined by the incident frequency, eliminating reconfiguration latency;
- their reduced architectural complexity offers the potential for scalable and cost-effective deployment, particularly at mmWave frequencies.

In the present work, the metaprism concept is implemented through a reflective passive smart electromagnetic skin operating at 28 GHz. The required dispersive phase profile is achieved by engineering the geometrical parameters of the unit cells, enabling deterministic frequency-dependent beam redirection without active circuitry.

1.4 State of Art

The Smart Radio Environment paradigm has shifted the role of the propagation medium from passive entity to controllable component of the wireless system [1]. Recent research has focused on engineered reflective surfaces capable of tailoring electromagnetic wavefronts in order to enhance coverage, improve link robustness, and enable new functionalities at millimeter-wave (mmWave) frequencies.

Metasurfaces constitute the technological foundation of this evolution. Following the theoretical formalization based on generalized sheet transition conditions [3] and the introduction of generalized reflection laws [6], significant

efforts have been devoted to practical implementations suitable for high-frequency applications. However, at mmWave frequencies, resonant unit cells—commonly employed to achieve full 2π phase coverage—introduce strong dispersion, reduced bandwidth, and increased sensitivity to losses and fabrication tolerances. These limitations remain critical in the 28 GHz band targeted by emerging 5G and 6G systems.

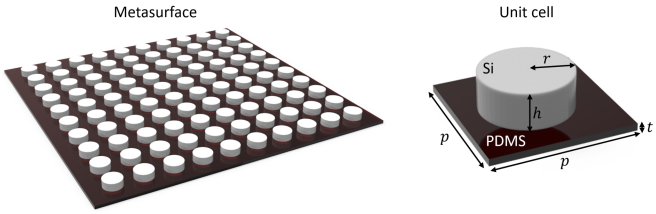

Figure 1.4: Conceptual illustration of a reflective metasurface with an example of Unit Cell [8]

To introduce adaptability, Reconfigurable Intelligent Surfaces (RIS) have integrated tunable elements within each unit cell, enabling dynamic beam steering and real-time link optimization [9, 1]. Although RIS architectures offer high flexibility, their practical implementation at mmWave frequencies entails bias networks, control circuitry, and distributed power systems, increasing hardware complexity and insertion losses. The integration of active components also raises concerns related to thermal management, scalability, and long-term reliability.

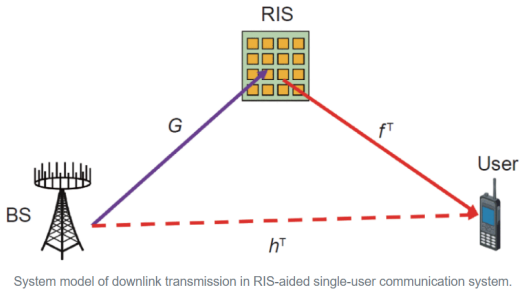

Figure 1.5: RIS Basic work principle[10]

In parallel, recent works have explored fully passive solutions under the framework of Smart Electromagnetic Skins (SES). Experimental demonstrations have shown that properly engineered passive reflective panels can

significantly enhance indoor and outdoor mmWave coverage without requiring active biasing. Transparent electromagnetic skins compatible with architectural integration have been proposed for outdoor-to-indoor enhancement [11], while passive SES implementations have experimentally validated coverage improvements in 5G indoor environments [12]. These studies confirm that phase-engineered passive reflectors can outperform conventional metallic plates of equal aperture.

Another research direction has investigated the controlled exploitation of unit-cell dispersion. Rather than attempting to mitigate frequency dependence, recent studies have proposed harnessing it as a design resource. The metaprism concept introduces reflective surfaces with a frequency-dependent phase gradient, enabling the angular separation of spectral components [13]. The potential of this beam steering for non-line-of-sight localization has been further explored in [14], as have its applications in near-field imaging in [15].

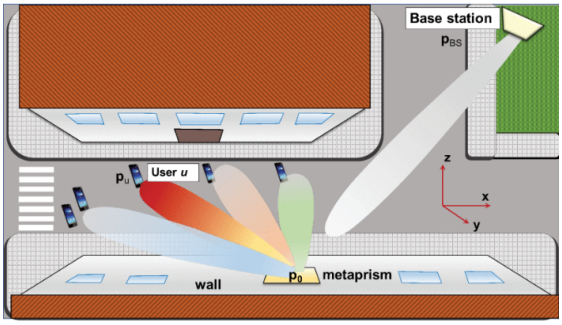

The considered NLOS scenario empowered by a metaprism.

Figure 1.6: Implementation of a metaprism [5]

Despite these advances, practical mmWave implementations of passive dispersive reflective skins remain limited. Existing approaches often rely on multilayer dielectric stacks or strongly resonant elements, which may reduce efficiency, narrow bandwidth, or increase fabrication complexity. Achieving controlled dispersive phase responses with high reflection efficiency and low-complexity unit-cell geometries at 28 GHz therefore remains an open challenge.

In this context, the present work investigates the design of a fully passive reflective smart electromagnetic skin operating at 28 GHz, with emphasis on low-complexity metallic unit cells capable of providing wide phase coverage and controlled metaprismatic dispersion.

1.5 Thesis Outline

This thesis set as objective the study and analysis of a metasurface-based metaprism operating in the range of mm-Waves, in particular around the 28GHz band. The 28 GHz frequency range is a key enabler for future wireless systems, offering a trade-off between bandwidth, achievable data rates and propagation range compared to higher mm-waves bands. The work will cover both design and simulation to evaluate a metaprism capable of controlling the phase reflected in response of an incident wave to achieve frequency dependent beam reflection. The basis for this is the definition of an ideal structure defined in [5], describing how a metaprism should work and what are the expected result. This thesis is divided as follows:

- Chapter 1: Introduction to Smart Radio Environments and to the concept of metaprism and Smart Electromagnetic Skins leading to the state of art works;
- Chapter 2: Unit Cell Design and Implementation, describing the first studies made on unit cells, leading to the one with the better reflection properties;
- Chapter 3:Design and Analysis of different smart skins, observing how feasible is a perfect metaprism;
- Chapter 4: Conclusions, final remarks of the results and future research.

Chapter 2

Unit Cell Design

The core objective of this thesis is the design of passive metaprisms based on resonant unit cells operating around 28 GHz. As introduced in the previous chapter, a metaprism is a non-reconfigurable reflective metasurface whose steering capability originates from the frequency-dependent phase response of its constituent elements. The global electromagnetic behavior of the structure therefore fundamentally depends on the local response of the individual unit cells. For this reason, the design process does not begin with the synthesis of the full metasurface, but with the rigorous electromagnetic characterization of a single periodic element. In reflective configurations, each unit cell behaves as a subwavelength scatterer engineered to impose a prescribed phase shift on the incident field while maintaining high reflection efficiency. By tailoring its geometrical parameters, it is possible to control the phase of the dominant reflected mode and thus determine the building blocks required for the metaprism implementation. A detailed analysis of the unit cell is therefore carried out with the objective of determining its phase coverage, dispersion characteristics, and robustness with respect to geometrical variations and incidence angle. In particular, special attention is devoted to the so-called S-curve, which relates the reflection phase to frequency and to selected geometrical parameters under different excitation conditions. Since the reflection phase generally depends on both frequency and angle of incidence, spatial dispersion effects must be carefully evaluated, especially in metaprism applications where frequency-dependent steering is intentionally exploited.

The electromagnetic response of the unit cell is rigorously described using the scattering matrix (S-matrix) formalism. In reflective metasurfaces backed

by a metallic ground plane, transmission is suppressed and the dominant parameter is the reflection coefficient S_{11}. Its magnitude and phase fully characterize the response of the cell under plane-wave excitation. While the magnitude is designed to remain close to unity in order to minimize dissipative losses, the reflection phase represents the primary degree of freedom exploited for wavefront control.

The characterization of the unit cell is performed under periodic boundary conditions in order to emulate an infinite two-dimensional array. This approach, based on Floquet theory, enables the study of a single element while accounting for mutual coupling effects inherent to periodic structures. The reflection phase extracted from the fundamental Floquet mode therefore constitutes the key design parameter for comparing different unit cell architectures.

Before introducing the specific unit cell architectures, the fundamental physical principle enabling wavefront manipulation in metasurfaces is briefly recalled.

2.1 Anomalous Reflection and Generalized Snell's Law

A key electromagnetic mechanism enabling wavefront manipulation in metasurfaces is anomalous reflection. In conventional reflection from a planar interface, the angle of reflection is equal to the angle of incidence, according to Snell's law. However, metasurfaces can introduce abrupt phase discontinuities along their surface, thereby modifying the reflection law.

When a spatially varying phase shift $\Phi(x)$ is imposed along the surface, the classical Snell's law must be generalized to account for the additional momentum provided by the phase gradient. The generalized law of reflection can be expressed as:

$$\sin\theta_r - \sin\theta_i = \frac{\lambda}{2\pi}\frac{d\Phi(x)}{dx} \tag{2.1}$$

where θ_i and θ_r denote the angles of incidence and reflection, respectively, λ is the wavelength, and $d\Phi/dx$ represents the phase gradient along the surface.

This relation shows that by engineering a suitable phase gradient, the reflected wave can be redirected toward arbitrary angles, independently of

the incidence angle. This phenomenon is referred to as anomalous reflection and constitutes the fundamental principle behind beam steering in reflective metasurfaces [6]. While conventional metasurfaces typically enforce a fixed phase gradient at a single frequency, metaprisms extend this concept by exploiting the intrinsic frequency dispersion of the unit cells. As a result, the phase gradient becomes frequency-dependent, leading to different reflection angles for different spectral components of the incident signal. The following sections introduce the periodic modeling framework adopted for the electromagnetic analysis and subsequently present the investigation of two different implementations: a dielectric cylindrical configuration and a metallic resonant structure.

2.2 Dielectric Cylindrical Unit Cell

The selection of the unit cell architecture is driven by the specific requirements imposed by metaprism operation. Unlike conventional reflective metasurfaces designed for single-frequency beam steering, metaprisms require unit cells capable of providing a controlled and predictable phase dispersion over frequency, while preserving high reflection efficiency and stability under oblique incidence. Dielectric resonant elements represent a suitable solution for this purpose. In contrast to planar metallic resonators, where phase control is mainly achieved through localized surface currents, dielectric structures rely on volumetric displacement currents and propagation effects within the dielectric body. This mechanism typically results in smoother phase transitions, reduced ohmic losses at millimeter-wave frequencies, and improved robustness against fabrication tolerances.

Among the possible dielectric geometries, the cylindrical configuration is particularly attractive due to its rotational symmetry. This symmetry mitigates polarization-dependent effects and enhances angular stability under normal incidence conditions. For these reasons, a dielectric cylindrical unit cell backed by a metallic ground plane is adopted, following the approach proposed in [16].

2.2.1 Geometry and Design Parameters

The implemented unit cell consists of a dielectric cylinder of radius r and height h, placed on a grounded dielectric substrate. The metallic ground plane suppresses transmission, ensuring that the electromagnetic response is fully characterized by the reflection coefficient S_{11}.

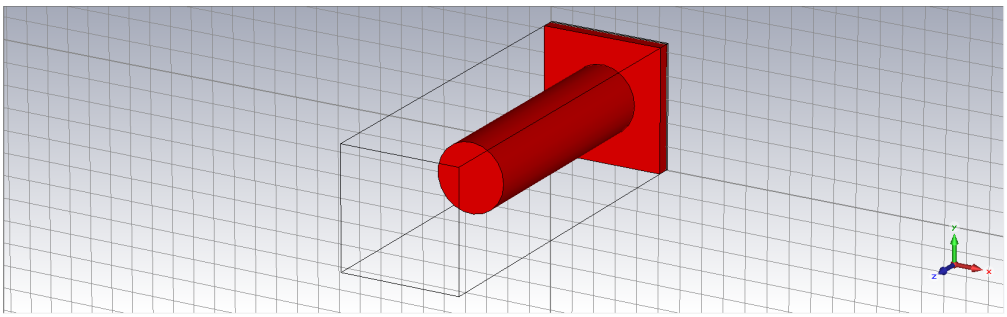

Figure 2.1: Geometry of the dielectric cylindrical unit cell backed by a metallic ground plane.

The dielectric material plays a fundamental role in determining the achievable phase range. A moderate-to-high relative permittivity enhances phase sensitivity with respect to geometrical variations, while avoiding excessively sharp resonances that could compromise bandwidth and stability. For this reason, Rogers RO3006 with relative permittivity $\varepsilon_r = 6$ is selected.

The unit cell is designed to operate around the central frequency

$$f_0 = 28 \text{ GHz}$$

with an operating bandwidth

$$27.8 \text{ GHz} \leq f \leq 28.2 \text{ GHz}.$$

At f_0, the free-space wavelength is

$$\lambda_0 \approx 10.7 \text{ mm}.$$

The lateral periodicity is chosen as

$$p = 0.4\,\lambda_0,$$

ensuring sub-wavelength spacing and aiming to suppress higher-order Floquet modes. This choice guarantees operation in a monomodal reflection regime and can justify the use of a local periodic approximation.

The cylinder radius is set to $r = 0.3\,\lambda_0$, while the height h is selected as the main tuning parameter. The electromagnetic characterization is carried out in CST Microwave Studio using unit cell boundary conditions along the transverse directions and Floquet ports along the propagation axis, as shown in Fig. 2.2. This configuration emulates an infinite metasurface illuminated by a normally incident plane wave.

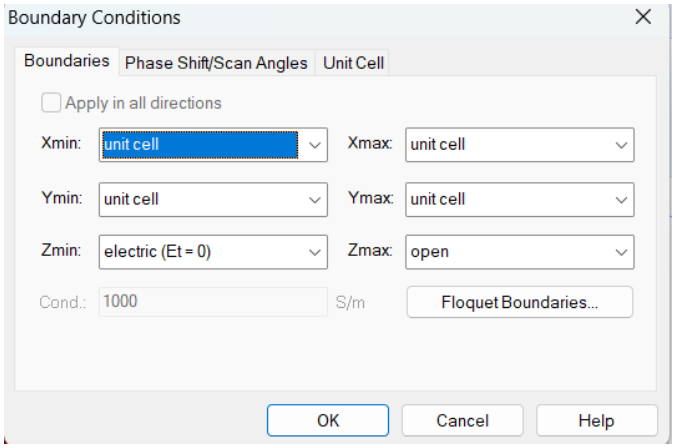

Figure 2.2: Simulation setup with periodic boundary conditions and Floquet ports.

For each geometrical configuration, the reflection coefficient S_{11} associated with the fundamental Floquet mode is plotted over the operating bandwidth. To evaluate the phase tunability of the unit cell, the cylinder height h is systematically varied while keeping all other parameters fixed in order to observe the impact of the change of the phase response.

Figure 2.3 reports the phase of the reflection coefficient S_{11} for different values of h. It can be observed how different values of h produce a set of phase responses that are approximately linear with frequency across the considered operating band. For each geometrical configuration, the phase exhibits a nearly constant slope, indicating a stable dispersive behavior of the unit cell. As h increases, the phase curves shift monotonically along values of phase, while maintaining a similar slope. This behaviour indicates that the cell geometry primarily controls the absolute phase delay introduced upon reflection, without significantly altering the dispersion characteristics of the structure.

From a physical perspective, this trend can be explained by considering that increasing the dielectric height effectively increases the electrical length of the resonant cavity. As a consequence, the electromagnetic wave experiences a longer propagation path inside the dielectric region before being reflected, which results in an additional phase delay. At the same time, a clear and quasi-monotonic phase shift is observed as h increases. Physically, increasing the dielectric thickness enhances the effective electrical path inside the resonator, resulting in an additional phase delay upon reflection. The reflection phase

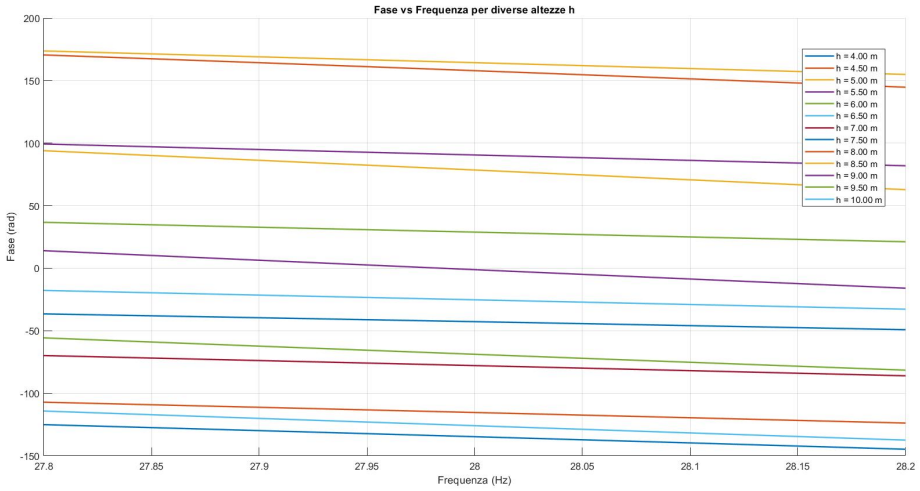

Figure 2.3: Phase of the reflection coefficient S_{11} of the dielectric unit cell for different values of the cylinder height.

at the central frequency f_0 is extracted for each configuration and reported in Fig. 2.4.

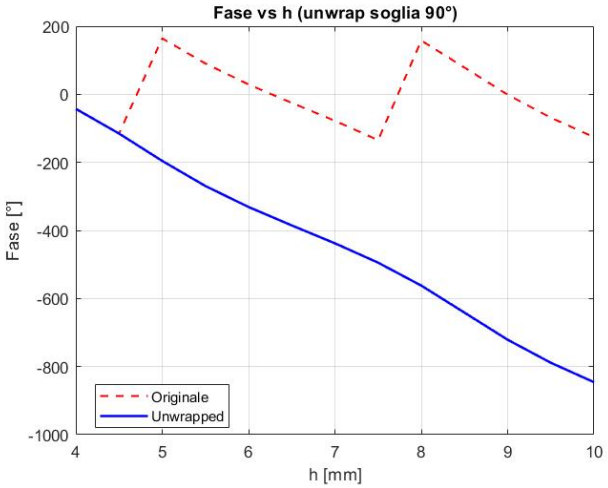

Figure 2.4: Reflection phase at $f_0 = 28$ GHz as a function of the cylinder height.

The resulting phase-versus-height curve establishes a one-to-one mapping between the geometrical parameter h and the achievable reflection phase.

The total phase excursion is approximately

$$\Delta\Phi = 330^\circ,$$

demonstrating that the cylinder height represents an effective and continuous tuning parameter suitable for metasurface phase synthesis.

The phase behavior exhibited a dependence on the cylinder height in a limited frequency range around 28 GHz. However, the achievable phase excursion within the operational bandwidth (27.8–28.2 GHz) was strongly influenced by resonance effects. In particular, the phase variation was concentrated in narrow frequency regions, resulting in increased sensitivity to geometrical tolerances and angular incidence.

For metaprism applications, where frequency-dependent steering relies on a predictable and robust phase dispersion, this resonant behavior represents a limitation. The phase coverage and dispersion characteristics obtained with the dielectric configuration were therefore considered insufficient to guarantee stable and controllable beam steering across the desired bandwidth.

For these reasons, an alternative unit cell architecture based on metallic waveguide propagation was investigated. In contrast to resonant dielectric elements, metallic waveguides operating near their cut-off frequency enable phase control through propagation mechanisms, offering enhanced tunability and smoother dispersion characteristics.

The following section presents the design and analysis of the proposed metal waveguide unit cell.

2.3 Metallic Waveguide Unit Cell

In order to realize propagation-based phase control, a metallic unit cell based on a square waveguide cavity is adopted. The structure consists of a square aperture of side length $a = 5.7$ mm periodically repeated with period $p = 6$ mm in a perfectly electrically conducting (PEC) slab where each aperture forms a square metallic waveguide cavity of length l_g . Unlike dielectric resonant elements, where the phase response is governed by localized energy storage, the present configuration exploits guided-wave propagation inside the metallic cavity. The reflection phase is therefore controlled by the accumulated propagation phase along the cavity length.

The square cavity behaves as a rectangular waveguide of dimensions $a \times a$. The cut-off frequency of the dominant TE_{10} mode is

$$f_c = \frac{c}{2a} \tag{2.2}$$

which, for $a = 5.7$ mm, yields

$$f_c \approx 26.3 \text{ GHz}. \tag{2.3}$$

Since the operating frequency is centered at $f_0 = 28$ GHz, the structure operates slightly above cut-off. This near cut-off regime is particularly advantageous because it results in strong dispersion and enhanced phase sensitivity, while still ensuring single-mode operation.

Above cut-off, the normalized longitudinal propagation constant is

$$k_{z,\mathrm{norm}} = \sqrt{1 - \left(\frac{f_c}{f}\right)^2} \tag{2.4}$$

and the actual longitudinal propagation constant becomes

$$k_z = k_0 \sqrt{1 - \left(\frac{f_c}{f}\right)^2} \tag{2.5}$$

where

$$k_0 = \frac{2\pi f}{v_f} \tag{2.6}$$

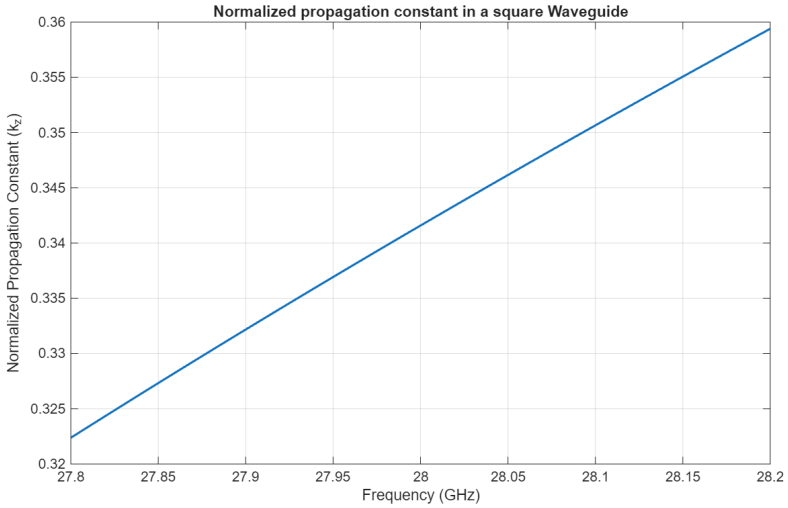

Figure 2.5: Normalized propagation constant $k_{z,\text{norm}}$ versus frequency.

and $v_f = \frac{c}{\sqrt{\varepsilon_r}}$ is the phase velocity inside the guide. Figure 2.5 shows the normalized propagation constant as a function of frequency within the considered bandwidth.

The guided wavelength inside the cavity is given by

$$\lambda_g = \frac{2\pi}{k_z}. \tag{2.7}$$

Near cut-off, $k_z \to 0$ and therefore $\lambda_g \to \infty$. This means that a relatively small variation of the cavity length produces a large phase variation, enabling wide phase tuning without relying on narrowband resonance phenomena.

The characteristic impedance of the dominant TE mode is

$$Z_c = \frac{Z_d}{\sqrt{1 - \left(\frac{f_c}{f}\right)^2}} \tag{2.8}$$

where

$$Z_d = \frac{Z_0}{\sqrt{\varepsilon_r}} \tag{2.9}$$

and $Z_0 = 120\pi$ is the free-space impedance. As the frequency approaches the cut-off, Z_c increases significantly, reinforcing the reactive nature of the cavity input impedance.

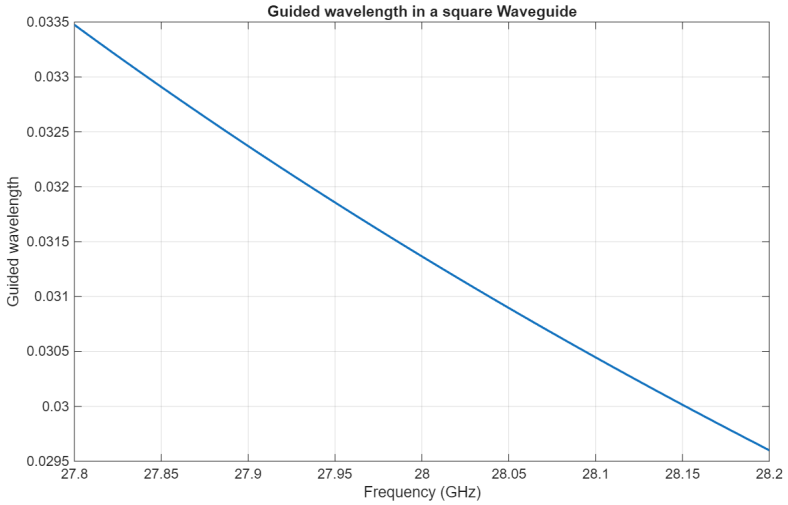

Figure 2.6: Guided wavelength λ_g versus frequency.

When the cavity is terminated by a PEC ground plane, the input impedance at the aperture can be modeled as a purely reactive impedance:

$$X_s = \frac{Z_c}{Z_0} \tan(k_z l_g). \tag{2.10}$$

The phase of the reflection coefficient can therefore be expressed as

$$\Phi(f, l_g) = 2 \arctan\left(X_s\right). \tag{2.11}$$

This expression provides a more accurate description than the simple approximation $\Phi \approx -2k_z l_g$, since it explicitly accounts for the impedance transformation occurring along the cavity.

For fixed cavity lengths, the phase variation with frequency becomes

$$\Phi(f) = 2 \arctan\left(\frac{Z_c(f)}{Z_0} \tan\left(k_z(f) l_g\right)\right). \tag{2.12}$$

Figure 2.7 shows the phase variation with frequency for different cavity lengths. A key observation emerges when comparing short and long guide configurations.

For relatively short guide lengths, the phase response exhibits an approximately linear behavior within the considered bandwidth around $f_0 = 28$

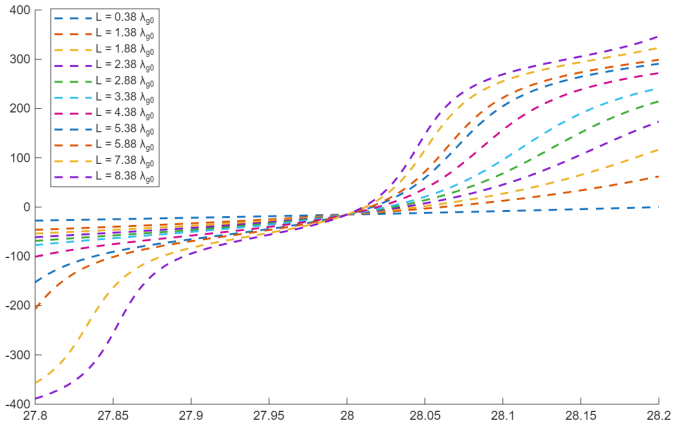

Figure 2.7: Phase variation versus frequency for different cavity lengths.

GHz. In this regime, the argument $k_z l_g$ remains sufficiently small such that the tangent function can be locally approximated as

$$\tan(k_z l_g) \approx k_z l_g. \tag{2.13}$$

Consequently, the surface reactance becomes approximately proportional to $k_z l_g$, and the reflection phase follows a quasi-linear frequency dependence. This regime is particularly advantageous for metasurface array synthesis, since it ensures a predictable and nearly uniform phase slope among adjacent elements. As the cavity length increases, the behavior progressively departs from linearity. When $k_z l_g$ approaches $\pi/2$, the tangent term grows rapidly and the phase response assumes a strongly nonlinear, tangent-like profile. In this regime, small frequency variations produce large phase excursions, resulting in enhanced dispersion and reduced predictability of the phase slope.

This transition from quasi-linear to tangent-like behavior is a direct consequence of the impedance transformation inside the cavity. While the mechanism remains purely propagation-based (i.e., no localized resonant storage is involved), long cavities operate closer to a reactive standing-wave condition, where the input reactance varies rapidly with frequency.

From a design perspective, this distinction is crucial:

- Shorter cavities provide smoother and more linear phase responses, ideal for uniform phase discretization.
- Longer cavities provide steeper phase excursions, enabling extended

phase coverage but at the expense of increased dispersion.

Therefore, the unit cell library used for the Smart Skin array is not selected arbitrarily. Instead, cavity lengths are chosen within the quasi-linear region whenever possible, ensuring stable phase spacing between adjacent elements while maintaining full 2π coverage.

This behavior, clearly visible in Fig. 2.7, represents one of the key physical insights of the proposed propagation-based metasurface design.

The analytical model derived above fully explains the propagation-based phase tuning mechanism of the metallic unit cell. Operating slightly above cut-off provides several distinctive propagation properties that directly impact the metasurface design.

Chapter 3

Smart Skin Designs And Different Analysis

The electromagnetic behavior of the single unit cell has been fully characterized in the previous chapter, demonstrating continuous phase tunability through propagation-based control inside square metallic waveguides. However, anomalous reflection is not a local phenomenon: it emerges from the coherent spatial distribution of phase across an extended aperture. When multiple unit cells are arranged to impose a linear phase gradient, the metasurface operates as a metaprism, converting local phase delays into a global redirection of the reflected wavefront. In this framework, the reflection angle is determined by the spatial phase derivative rather than by the response of an individual element. In an ideal continuous model, a perfectly linear phase profile extending over an infinite aperture produces a well-defined reflected beam whose direction follows the generalized law of reflection. In practice, the metasurface is composed of a finite and discretized set of unit cells. Unlike the ideal continuous model, the Smart Skin array exhibits a limited electrical aperture and spatial sampling density, which directly affect beam formation and reflection efficiency. Consequently, the ability of the structure to operate as a true frequency-scanning metaprism depends on the number of cells employed and on their collective electromagnetic interaction. The key design parameter of the array is the phase distribution required to produce anomalous reflection, which is derived from the Generalized Snell's Law. For an incident angle θ_i and reflection angle θ_r, the imposed phase gradient must satisfy

$$k_0 \left(\sin\theta_r - \sin\theta_i\right) = \frac{d\Phi(x)}{dx} \tag{3.1}$$

where $k_0 = 2\pi/\lambda_0$ is the free-space wavenumber.

For a discretized metasurface with periodicity p, the required phase increment between adjacent cells becomes

$$\Delta\Phi = k_0 p \left(\sin\theta_r - \sin\theta_i\right). \tag{3.2}$$

At $f_0 = 28$ GHz, with $\lambda_0 = 10.71$ mm, the phase step is fully determined by the imposed geometry and steering requirement.

The spatial length required to accumulate a full 2π phase rotation is

$$L_{2\pi} = \frac{2\pi}{\frac{d\Phi}{dx}} = \frac{\lambda_0}{\sin\theta_r - \sin\theta_i}. \tag{3.3}$$

The minimum number of unit cells necessary to cover a full 2π phase excursion is therefore

$$N_{\min} = \frac{L_{2\pi}}{p}. \tag{3.4}$$

This analytical estimation provides the lower bound for phase discretization. The required phase distribution is physically implemented by selecting the cavity heights according to the propagation-based phase model discussed in Chapter 2. The continuous phase gradient is therefore approximated through a discrete set of unit cells spaced by the periodicity p. Although the analytical formulation establishes the theoretical phase-gradient requirement, the real electromagnetic response must be validated for finite array dimensions. Therefore, a systematic full-wave investigation is required.

The objective of this chapter is to demonstrate that the reflective metasurface based on square metallic waveguides is capable of implementing the desired anomalous reflection predicted by the Generalized Snell's Law.

The design frequency is $f_{\text{des}} = 28$ GHz and the target reflection angle under normal incidence is $\phi_o = 17.5°$. The metasurface is composed of $N_y \times N_z$ unit cells arranged along the transverse directions, with periodicity d.

Rather than directly validating the full-wave structure, a hierarchical modeling strategy is adopted. Three progressively more realistic models are considered:

1. An ideal phase-imposed array (discussed here [5]),
2. A physically consistent transmission-line (TL) model of the square waveguide cell,
3. A full-wave electromagnetic simulation performed in CST Studio.

This multi-level comparison allows separating:

- Ideal beamforming behavior,
- Physical phase implementation limits,
- Full-wave electromagnetic coupling effects.

3.0.1 Ideal Phase-Imposed Array

The theoretical foundation of the metasurface design adopted in this work is based on the metaprism concept introduced in [5]. In this framework, the metasurface is designed to impose a phase distribution that varies linearly both in space and frequency. Such a behavior enables controlled beam steering and frequency–angle mapping, which represents the key operating principle of metaprisms. In a conventional phase-gradient metasurface the phase profile is typically designed for a single frequency. However, in the metaprism formulation the goal is to enforce a frequency-dependent phase distribution, enabling the metasurface to map different frequencies into different reflection angles.

For this reason, the phase distribution is expanded around the design frequency f_{des}, leading to the following approximation

$$\Phi(y, z, f) \approx \Phi(y, z, f_{des}) + (f - f_{des})\frac{\partial \Phi}{\partial f}. \tag{3.5}$$

By explicitly evaluating the frequency derivative of the phase, [5] shows that the phase variation with respect to frequency can be written as a linear function of the spatial coordinates. This leads to the phase-delay expression reported in Eq. (20) of [5]:

$$\Delta\Phi(y, z, f) = (a_0 y + b_0 z)\,(f - f_{des}) \tag{3.6}$$

where the coefficients a_0 and b_0 depend only on the incident and reflected directions

$$a_0 = -\frac{4\pi}{\lambda_{des} B_W}\,(\sin\phi_o \sin\theta_o + \sin\phi_i \sin\theta_i) \tag{3.7}$$

$$b_0 = -\frac{4\pi}{\lambda_{des} B_W}\,(\cos\theta_o + \cos\theta_i) \tag{3.8}$$

with λ_{des} the wavelength at the design frequency and B_W the considered bandwidth.

This equation states that the phase delay required at each metasurface position varies linearly with both spatial coordinates and operating frequency. As a consequence, different frequencies experience different effective phase gradients, which results in a controlled angular dispersion of the reflected beam.

This property is exploited in the present work in order to design a reflective metasurface capable of steering the reflected wave at a target angle while preserving a predictable frequency-dependent behavior.

3.0.2 Transmission-Line Model of the Square Waveguide Unit Cell

While the ideal metaprism model assumes that each unit cell can impose an arbitrary phase delay, a practical implementation requires a physical structure capable of reproducing the desired phase distribution. In this work the phase control is realized using metallic square waveguide cavities of different heights, each acting as a reflective phase shifter.

From an electromagnetic perspective, each unit cell can be modeled as a short-circuited section of rectangular waveguide. When a plane wave impinges on the metasurface, the electromagnetic field couples into the cavity and propagates along the waveguide until it reaches the metallic short circuit located at the bottom of the structure. The reflected wave then propagates back toward the aperture, producing a phase delay determined by the propagation constant of the guided mode and the cavity length.

This behavior can be accurately described using a transmission line equivalent model. Under the dominant mode approximation, the phase shift introduced by a waveguide cavity of height h can be written as

$$\Phi(h, f) = -2\beta(f)h \tag{3.9}$$

where $\beta(f)$ represents the propagation constant of the fundamental waveguide mode and the factor of two accounts for the round-trip propagation inside the cavity.

For a rectangular waveguide operating in the dominant TE_{10} mode, the propagation constant is given by

$$\beta(f) = \sqrt{k_0^2 - k_c^2} \tag{3.10}$$

where $k_0 = 2\pi/\lambda$ is the free-space wavenumber and k_c is the cutoff wavenumber of the waveguide mode.

The cutoff wavenumber depends on the waveguide dimensions and can be expressed as

$$k_c = \frac{2\pi}{a} \tag{3.11}$$

where a denotes the width of the square waveguide cross section.

Combining these expressions, the phase delay introduced by the cavity becomes

$$\Phi(h, f) = -2h\sqrt{\left(\frac{2\pi}{\lambda}\right)^2 - \left(\frac{2\pi}{a}\right)^2}. \tag{3.12}$$

This relation establishes a direct mapping between the physical height of the cavity and the reflection phase of the unit cell. By properly selecting the cavity length h, it is therefore possible to reproduce the discrete phase values required by the metasurface design. Using this phase distribution, the far-field is recomputed through the same array summation formula used in the ideal model, replacing Φ_{nm} with the phase obtained from the TL model.

This step allows quantifying the deviation introduced by:

- Finite phase resolution,
- Waveguide dispersion,
- Non-ideal phase linearity versus height.

3.0.3 Full-Wave CST Validation

The final level of validation of the proposed metasurface design is performed through full-wave electromagnetic simulations carried out using CST Microwave Studio.

While the ideal metaprism formulation and the transmission line model provide analytical and semi-analytical predictions of the metasurface response, they rely on simplifying assumptions such as independent unit cell behavior and idealized phase control. A full-wave simulation is therefore required in order to accurately capture the electromagnetic interactions occurring within the complete structure.

In particular, CST simulations allow accounting for several physical effects that are not included in the simplified models, such as mutual coupling between adjacent unit cells, edge diffraction phenomena due to the finite aperture, and higher-order modal interactions inside the waveguide cavities.

The complete metasurface structure is modeled by arranging the waveguide unit cells according to the phase distribution derived from the metaprism theory. Each unit cell corresponds to a square metallic cavity with height selected to reproduce the discrete phase values predicted by the transmission line model.

The metasurface is illuminated by a normally incident plane wave at the design frequency of 28 GHz. Open boundary conditions are applied in order to emulate free-space propagation, and far-field monitors are used to extract the bistatic Radar Cross Section (RCS) of the structure.

The simulated far-field pattern is used to evaluate the angular direction of maximum reflected radiation. This quantity is determined by identifying the angular position corresponding to the maximum value of the RCS pattern

$$\phi_{\max} = \arg\max_{\phi} \{\mathrm{RCS}(\phi)\} . \tag{3.13}$$

The CST results are then post-processed in order to reconstruct the complete angular range and align the simulation data with the analytical predictions obtained from the metaprism and transmission line models.

This procedure enables a direct comparison between the three modeling approaches considered in this work.

3.0.4 Comparative Analysis of the Three Models

The comparison among the three modeling levels provides a comprehensive understanding of the metasurface behavior and allows evaluating the accuracy of the proposed physical implementation.

The three considered models represent increasing levels of physical realism:

- the **ideal metaprism model**, which assumes perfect phase control according to the analytical phase law derived in Section 3.0.1;
- the **transmission line model**, which approximates the phase response of the waveguide cavities using guided-wave propagation theory;
- the **full-wave CST simulation**, which captures the complete electromagnetic response of the metasurface structure.

The comparison between the three models is discussed in detail in the following section, where different metasurface configurations are analyzed.

3.1 6-Cell Smart Skin

3.1.1 Geometrical Configuration and Phase Sampling

The 6-cell configuration represents the lowest discretization level considered in this work. In this case the 2π phase cycle is sampled using only six elements, resulting in phase increments of approximately 60° between adjacent cells considering a starting point of 0° at the center of the waveguide cavity. Such a coarse discretization introduces significant limitations in the capability of the metasurface to approximate the continuous phase gradient required by the ideal metaprism model. Because the phase variation along the surface is implemented through a limited number of discrete steps, the spatial sampling of the phase profile becomes relatively sparse. This reduced sampling density produces two main effects.
First, the effective phase gradient deviates from the ideal continuous distribution.
Second, the large phase difference between adjacent elements introduces stronger discretization artifacts in the reflected field. The total aperture length is $L = 6p$, where p is the unit-cell periodicity. Figure 3.1 shows the CST model of the 6-cell Smart Skin.

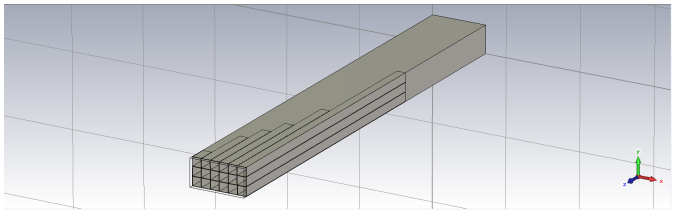

Figure 3.1: CST model of the 6-cell Smart Skin configuration.

The selected heights are displayed in Table 3.1

Table 3.1: Selected cavity heights for the 6-cell metasurface.

Cell Index	Height h [mm]
1	12.06
2	43.429
3	59.112
4	74.795
5	106.16
6	184.577

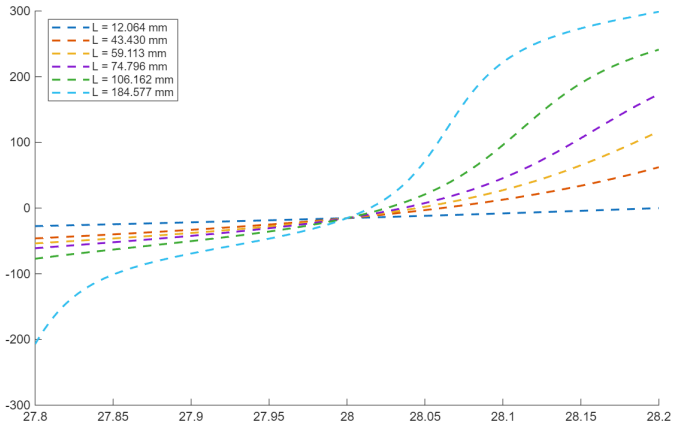

Figure 3.2: Phase response of the chosen lengths

Figure 3.2 shows the phase of S_{11} for the selected cavity lengths, which together cover the full 2π phase range. The result of the analysis for this configuration are exhibited below, as plots of the RCS for key points in the chosen frequency range of $28 - 28.2$ GHz

3.1.2 Frequency Evolution of the Reflection Pattern

To evaluate the beam steering capability of the 6-cell metasurface, the bistatic RCS pattern has been analyzed at several frequencies within the considered operating band.

Figure 3.3 shows the angular RCS distribution obtained from CST simulations between 28 GHz and 28.2 GHz.

The following table displays the maximum values of RCS for each case to facilitate an understanding of the analysis.

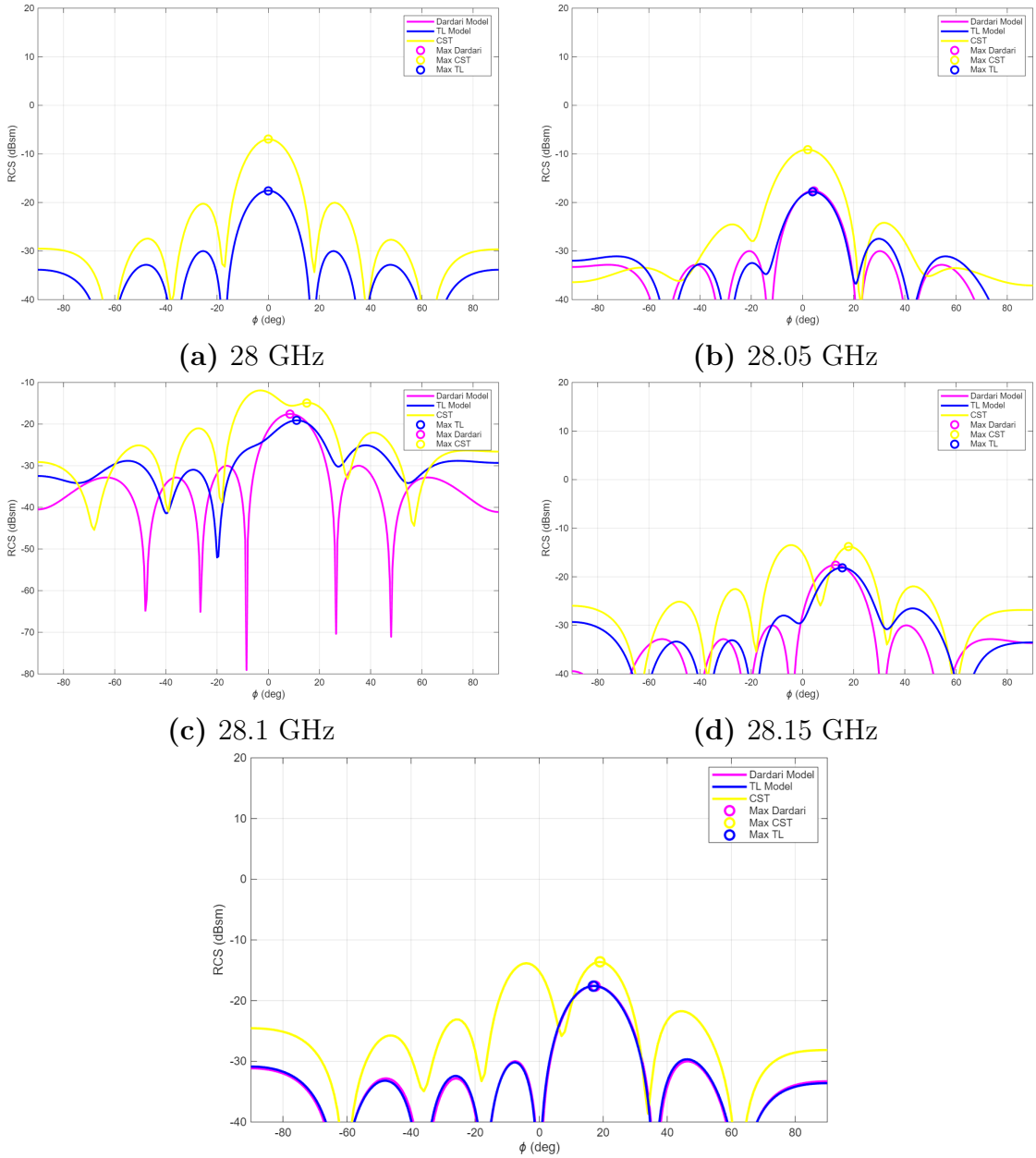

(a) 28 GHz **(b)** 28.05 GHz

(c) 28.1 GHz **(d)** 28.15 GHz

(e) 28.2 GHz

Figure 3.3: Bistatic RCS of the 6-cell smart skin for different frequencies in the selected bandwidth.

Table 3.2: Main reflection angle obtained by the three models for the 6-cell configuration.

Frequency [GHz]	Ideal Model	TL Model	CST Simulation
28.00	0	0	0
28.05	4.5	4	2
28.10	8.5	11	15
28.15	13	15.5	18
28.20	17.5	17	19

The radiation patterns show that the anomalous reflection lobe appears only at the upper part of the considered frequency range, while the specular reflection component remains dominant for lower frequencies.

This behavior indicates that the effective phase gradient implemented by the metasurface is not sufficiently uniform across the aperture. As a consequence, the beam steering mechanism predicted by the ideal metaprism model is only partially reproduced.

3.1.3 Phase Gradient Analysis

To better understand the electromagnetic behavior of the 6-cell metasurface, the spatial phase delay along the aperture has been analyzed.

Figure 3.4 shows the phase delay distribution obtained from the ideal model, the transmission line approximation, and the CST simulations for different operating frequencies.

The ideal metaprism model exhibits a perfectly linear phase profile along the surface, corresponding to a constant phase gradient.

The CST simulations instead reveal a strongly discretized phase distribution due to the limited number of elements. The phase difference between adjacent cells becomes relatively large, which prevents the metasurface from approximating the continuous phase gradient assumed in the analytical model.

These deviations explain the irregular beam steering behavior observed in the RCS patterns.

3.1.4 Discussion

The results obtained for the 6-cell configuration highlight the importance of the spatial sampling density in metasurface-based beam steering devices.

Although the metasurface is capable of producing anomalous reflection at the design frequency, the coarse phase discretization limits the ability of the structure to maintain a stable phase gradient across the operating band.

Consequently, the desired linear relationship between frequency and reflection angle predicted by the ideal metaprism model is not achieved.

These limitations motivate the investigation of metasurfaces with a larger number of elements, which allow a finer approximation of the continuous phase profile.

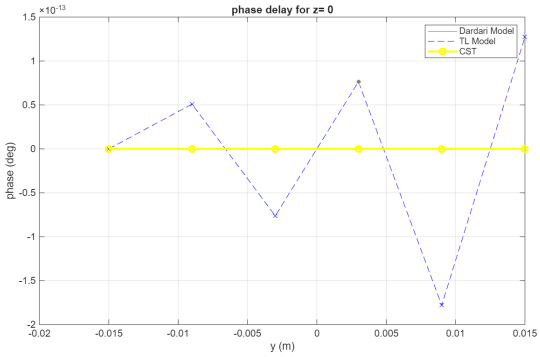

(a) 28 GHz

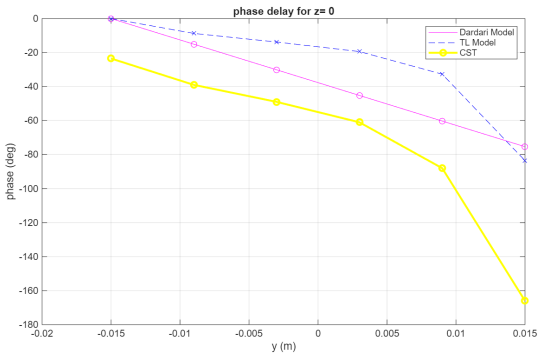

(b) 28.05 GHz

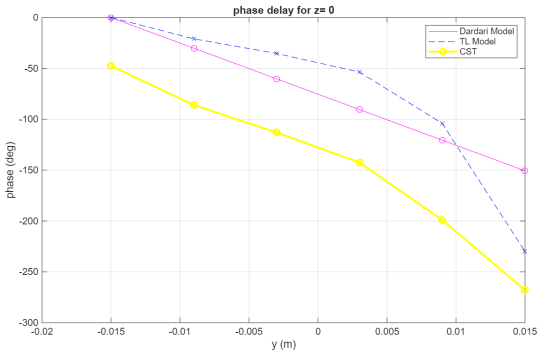

(c) 28.1 GHz

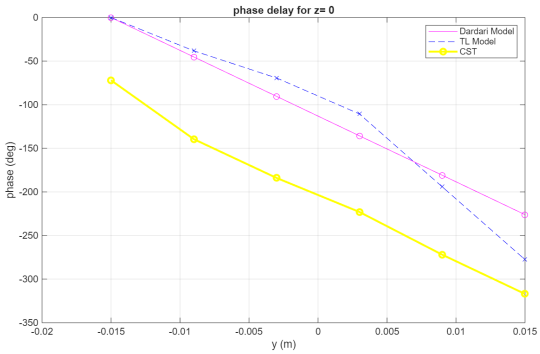

(d) 28.15 GHz

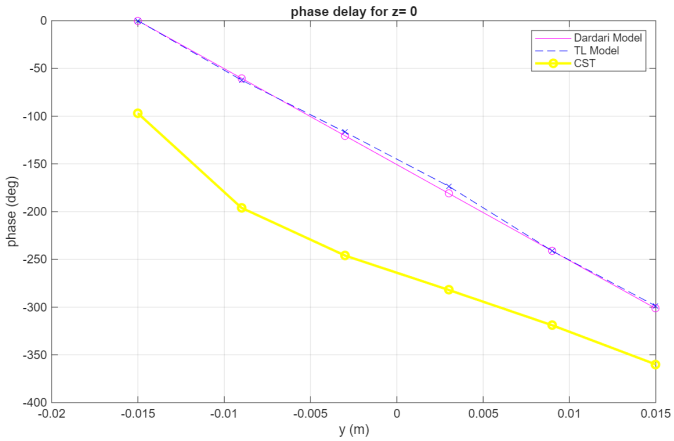

(e) 28.2 GHz

Figure 3.4: Spatial phase delay along the 6-cell metasurface.

3.2 7-Cell Smart Skin

3.2.1 Geometrical Configuration and Phase Sampling

The choice of seven elements represents the minimum practical discretization capable of reproducing a complete 2π phase cycle while maintaining a symmetric sampling of the phase profile.

In the ideal metaprism formulation, the phase gradient is continuous along the surface. However, in practical metasurfaces the phase distribution can only be implemented through a finite number of discrete unit cells, each providing a specific reflection phase.

This discretization introduces two main effects:

- spatial sampling of the phase gradient,
- phase quantization errors.

The spatial sampling determines how accurately the continuous phase function can be approximated, while the phase quantization limits the resolution of the achievable phase values.

In the present configuration the 2π phase cycle is sampled using $60°$ phase steps, which represent a relatively coarse discretization. This configuration therefore provides a useful baseline for evaluating the impact of limited phase resolution on the metaprism behavior. Figure 3.5 shows the complete CST model of the structure.

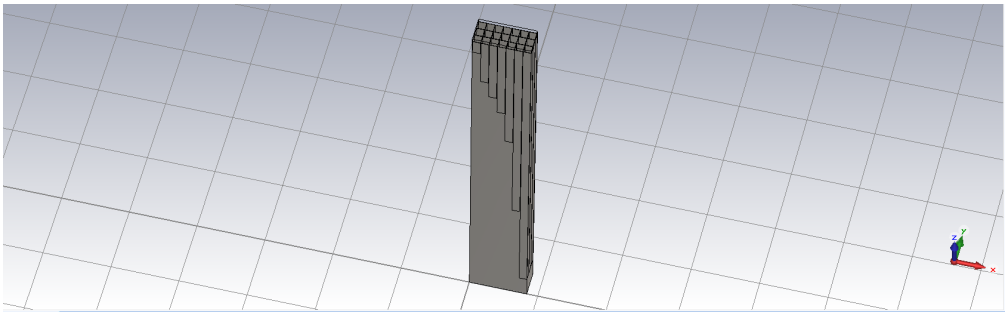

Figure 3.5: CST model of the 7-cell Smart Skin configuration.

The selected heights are displayed in Table 3.3

Table 3.3: Selected cavity heights for the 7-cell metasurface.

Cell Index	Height h [mm]
1	12.06
2	43.429
3	59.112
4	74.795
5	106.16
6	184.577
7	262.99

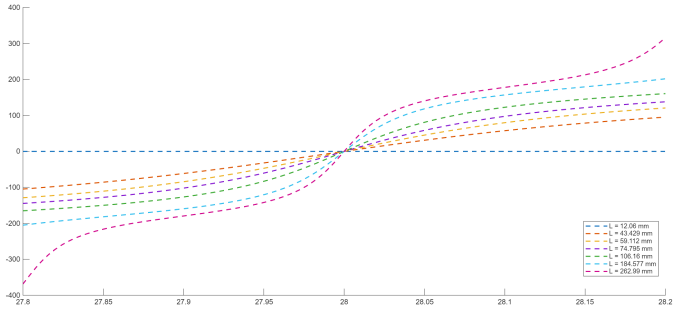

Figure 3.6: S11 Phase of the chosen lengths

The selected cavity heights and corresponding phase values at 28 GHz are summarized in Table 3.4 and shown in figure 3.6.

Table 3.4: Selected cavity heights and phase values at 28 GHz.

Cell Index	Height h [mm]	Phase at 28 GHz [deg]
1	12.06	0°
2	43.429	60°
3	59.112	114°
4	74.795	179°
5	106.16	240°
6	184.577	297°
7	262.99	344°

The total aperture length is $L = 7p$, where p is the unit-cell periodicity.

3.2.2 Frequency Evolution of the Reflection Pattern

The metaprism concept predicts that the reflection angle varies continuously with frequency due to the frequency-dependent phase delay introduced by the metasurface elements.

In the metaprism model introduced in [5], the phase delay imposed by each element follows a linear dependence with both spatial position and frequency. As a consequence, the phase gradient along the surface becomes frequency dependent, producing a progressive variation of the reflection angle.

Assuming a linear phase profile along the metasurface, the reflection angle can be expressed as

$$\sin\theta_r(f) = \frac{\lambda(f)}{2\pi p}\Delta\Phi(f) \tag{3.14}$$

where $\Delta\Phi(f)$ represents the frequency-dependent phase increment between adjacent cells.

If the phase response of each unit cell varies approximately linearly with frequency, the phase gradient remains approximately constant over the operating band. Under these conditions, the reflection angle varies smoothly with frequency, producing the characteristic beam-steering behavior of metaprisms.

To investigate this behavior, the bistatic RCS pattern of the 7-cell metasurface has been evaluated at several frequencies within the considered bandwidth.

Figure 3.7 show the angular RCS distribution for different frequencies between 28 GHz and 28.2 GHz.

Table 3.5: Main reflection angle obtained by the three models for the 7-cell configuration.

Frequency [GHz]	Ideal Model	TL Model	CST Simulation
28.00	0	0	0
28.05	4.5	6.5	0
28.10	8.5	15	16
28.15	13	15.5	17
28.20	17.5	16	17

A direct comparison between the three modeling approaches provides important insight into the physical mechanisms governing the metasurface behavior.

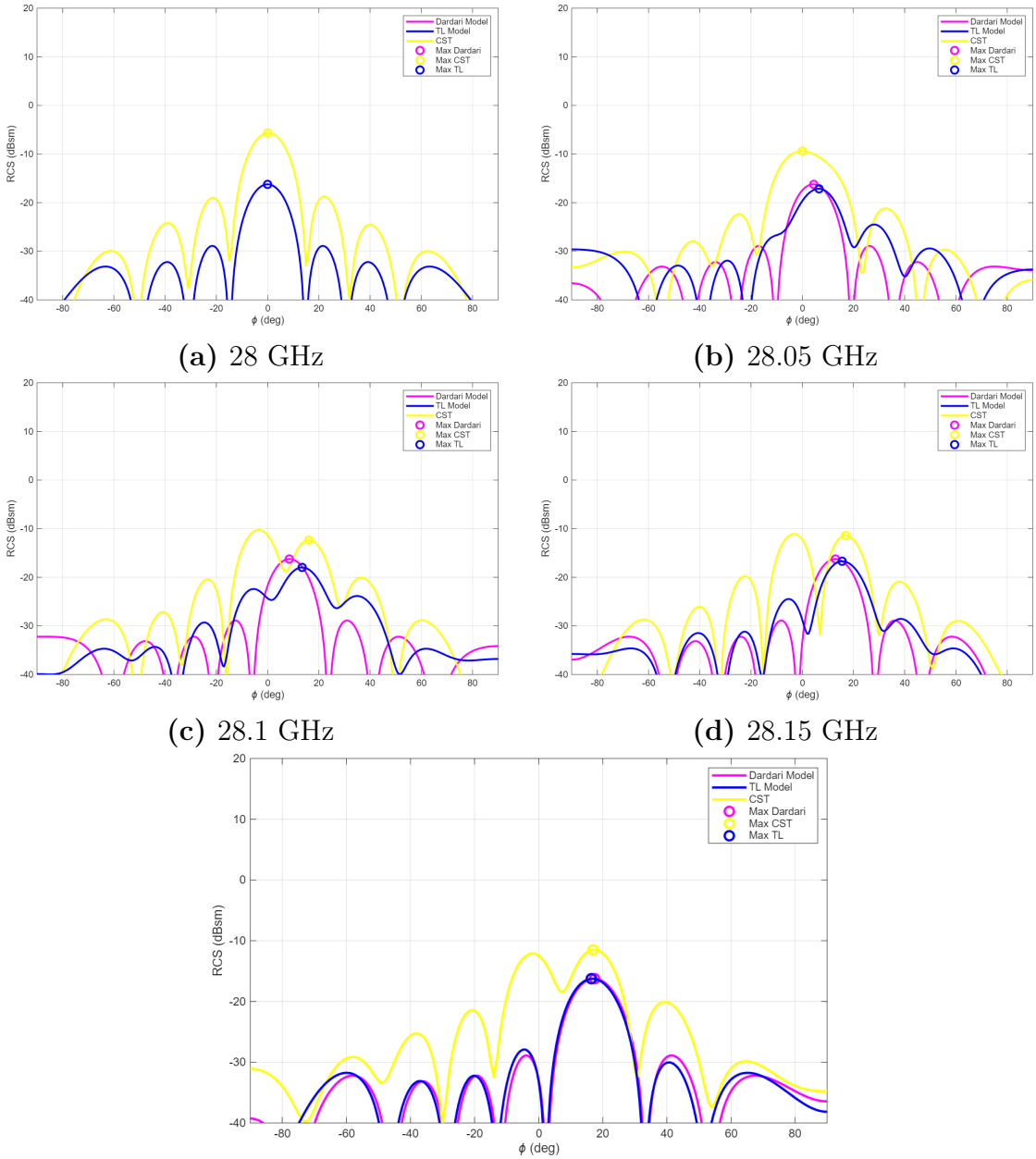

(a) 28 GHz **(b)** 28.05 GHz

(c) 28.1 GHz **(d)** 28.15 GHz

(e) 28.2 GHz

Figure 3.7: Bistatic RCS of the 7-cell smart skin for different frequencies in the selected bandwidth.

In the ideal metaprism model, the reflection lobe exhibits a nearly linear angular translation as the frequency increases from 28 GHz to 28.2 GHz.

The main lobe progressively shifts away from the specular direction, reaching approximately 17° at 28.2 GHz, in agreement with the theoretical prediction imposed by the phase gradient.

This behavior represents the target operation of the metaprism concept, where the metasurface converts a frequency variation into a controlled angular deviation of the reflected beam.

The transmission line model exhibits a noticeably different behavior. At 28 GHz the dominant reflection lobe remains close to the specular direction (0°), indicating that the effective phase gradient produced by the physical cavities differs from the ideal design value. As the frequency increases, the main lobe jumps at around 28.1 GHz at around 14°–15°, eventually reaching the designed reflection of 17° near the upper edge of the band.

This discontinuous transition indicates that the phase response of the waveguide cavities does not evolve linearly with frequency, leading to a non-uniform phase gradient across the surface.

The CST full-wave simulation reveals an even more pronounced deviation from the ideal behavior. The radiation pattern shows a stronger contribution from the specular reflection, and the transition toward the anomalous reflection direction occurs abruptly rather than continuously.

This behavior can be attributed to several electromagnetic effects that are not captured by the simplified models, including:

- mutual coupling between adjacent cavities,
- finite aperture truncation,
- diffraction from the array edges,
- higher-order modal contributions inside the cavities.

As a consequence, the expected linear angular translation of the reflection lobe is not fully achieved in the 7-cell configuration.

3.2.3 Phase Gradient Analysis

To further understand the beam steering behavior observed in the RCS simulations, the spatial phase distribution along the metasurface is analyzed. According to the metaprism formulation, anomalous reflection is obtained by imposing a linear phase gradient across the surface. In the ideal case, this corresponds to a constant phase increment between adjacent elements.

Figure 3.8 shows the spatial phase delay along the 7-cell metasurface for different operating frequencies, comparing the ideal metaprism model, the transmission line approximation, and the CST full-wave simulation.

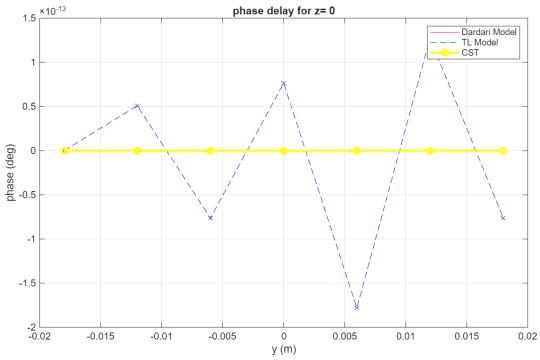

(a) 28 GHz

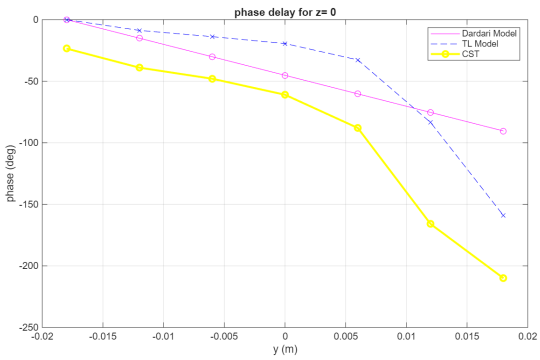

(b) 28.05 GHz

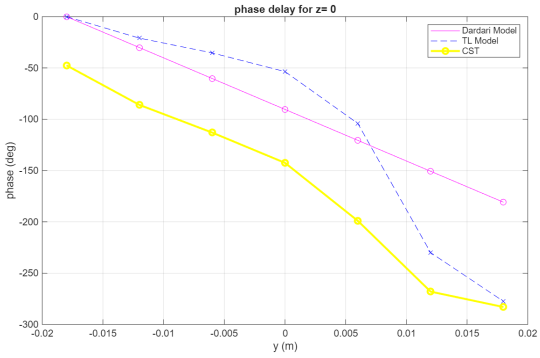

(c) 28.1 GHz

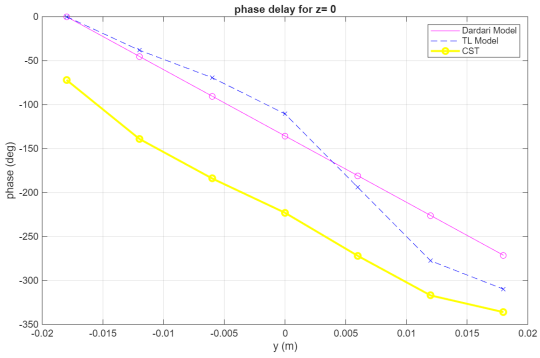

(d) 28.15 GHz

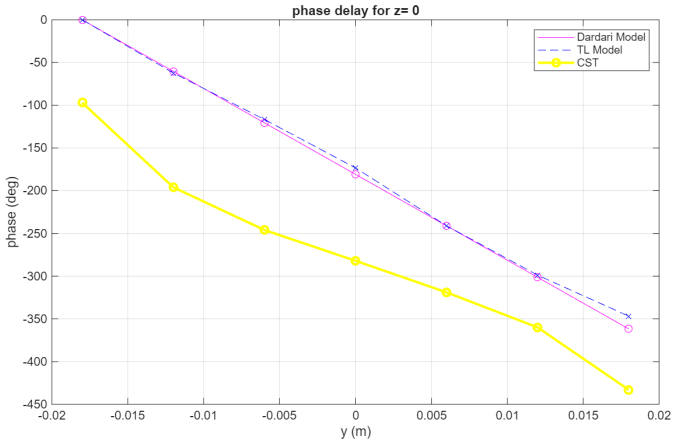

(e) 28.2 GHz

Figure 3.8: Spatial phase delay along the 7-cell metasurface for different frequencies.

The ideal model exhibits a perfectly linear phase profile along the surface, which corresponds to the constant phase gradient required to produce controlled beam steering.

The transmission line model follows a similar trend but introduces small deviations due to the dispersive propagation inside the cavities.

The CST simulations show a more irregular phase distribution. Because the phase cycle is distributed over a limited number of elements, the phase difference between adjacent cells becomes relatively large.

This coarse spatial sampling results in a discretized phase gradient that deviates from the continuous distribution assumed in the analytical model. As a consequence, the reflected beam exhibits the abrupt transitions observed in the RCS simulations when the operating frequency varies.

3.2.4 Discussion and Limitations of the 7-Cell Configuration

Although the 7-cell Smart Skin correctly reproduces the target anomalous reflection at the design frequency, its capability to reproduce the desired linear angular translation over frequency is limited.

The discrete phase sampling results in insufficient spatial resolution to maintain a linear phase gradient over the entire frequency range. Consequently, the RCS lobe does not exhibit the desired continuous angular translation predicted by the ideal model.

This behavior indicates that the aperture sampling density is insufficient to ensure frequency-consistent anomalous reflection. For this reason, the array is progressively refined by increasing the number of cells, leading to the 12-cell configuration discussed in the next section, using as a base the structure of the 6-cell configuration.

3.3 12-Cell Smart Skin

3.3.1 Motivation for Increasing the Number of Cells

The analysis of the 7-cell configuration showed that the coarse spatial sampling of the phase gradient significantly affects the beam steering behavior of the metasurface.

In particular, the relatively large phase difference between adjacent elements introduces phase quantization effects that prevent the structure from

accurately reproducing the continuous phase gradient assumed in the ideal metaprism model.

To reduce these limitations, the number of unit cells is increased to 12. By introducing additional elements along the metasurface aperture, the phase gradient can be sampled more finely, decreasing the phase step between neighboring cells and reducing the specular reflection.

This improvement is expected to produce a smoother angular evolution of the reflected beam as the operating frequency varies, allowing the metasurface to better approximate the ideal metaprism behavior.

The objective of this section is therefore to investigate how the increase in the number of cells affects the beam steering mechanism and the frequency stability of the reflected beam.

3.3.2 Array Geometry

The 12-cell metasurface is obtained by extending the phase gradient implemented in the 6-cell configuration while preserving the same unit-cell design and periodicity p.

The total aperture length becomes

$$L = 12p \tag{3.15}$$

which represents a substantial increase with respect to the 7-cell configuration.

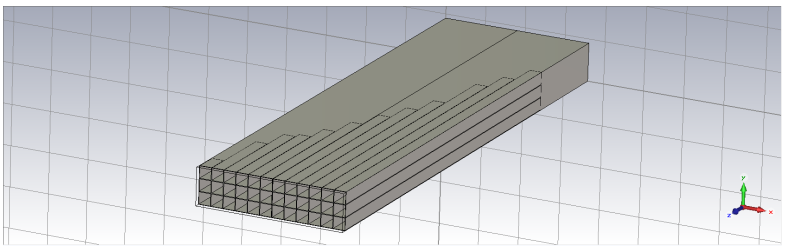

Figure 3.9: CST model of the 12-cell Smart Skin metasurface.

The selected heights are displayed in Table 3.6

Table 3.6: Selected cavity heights for the 12-cell metasurface.

Cell Index	Height h [mm]
1	12.06
2	27.74
3	43.429
4	59.112
5	74.795
6	90.48
7	106.16
8	121.85
9	137.53
10	168.89
11	184.577
12	200.26

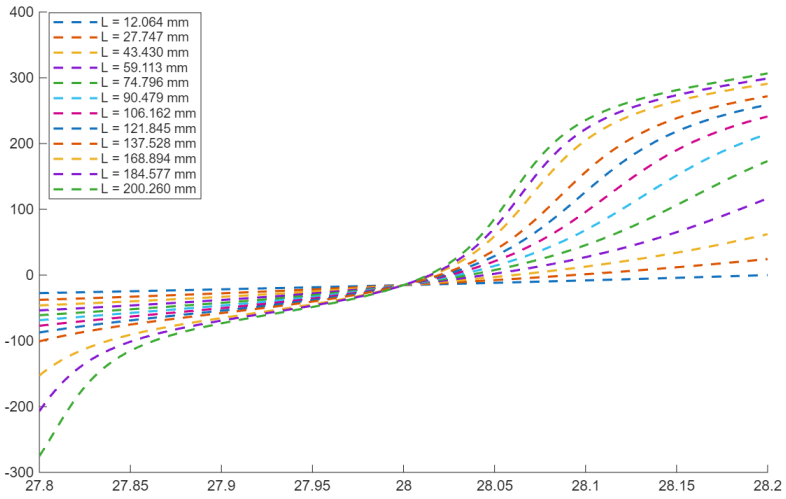

Figure 3.10: Phase response of the Unit Cell for the selected lengths

The larger aperture provides a better spatial sampling of the phase gradient and improves the angular resolution of the reflected radiation pattern.

At the same time, the increased number of elements reduces the phase discontinuities between adjacent cells, allowing the metasurface to more closely approximate the desired linear phase distribution.

3.3.3 Frequency Evolution of the Reflection Pattern

To evaluate the frequency-dependent behavior of the metasurface, the RCS pattern is computed at several frequencies between 28 GHz and 28.2 GHz.

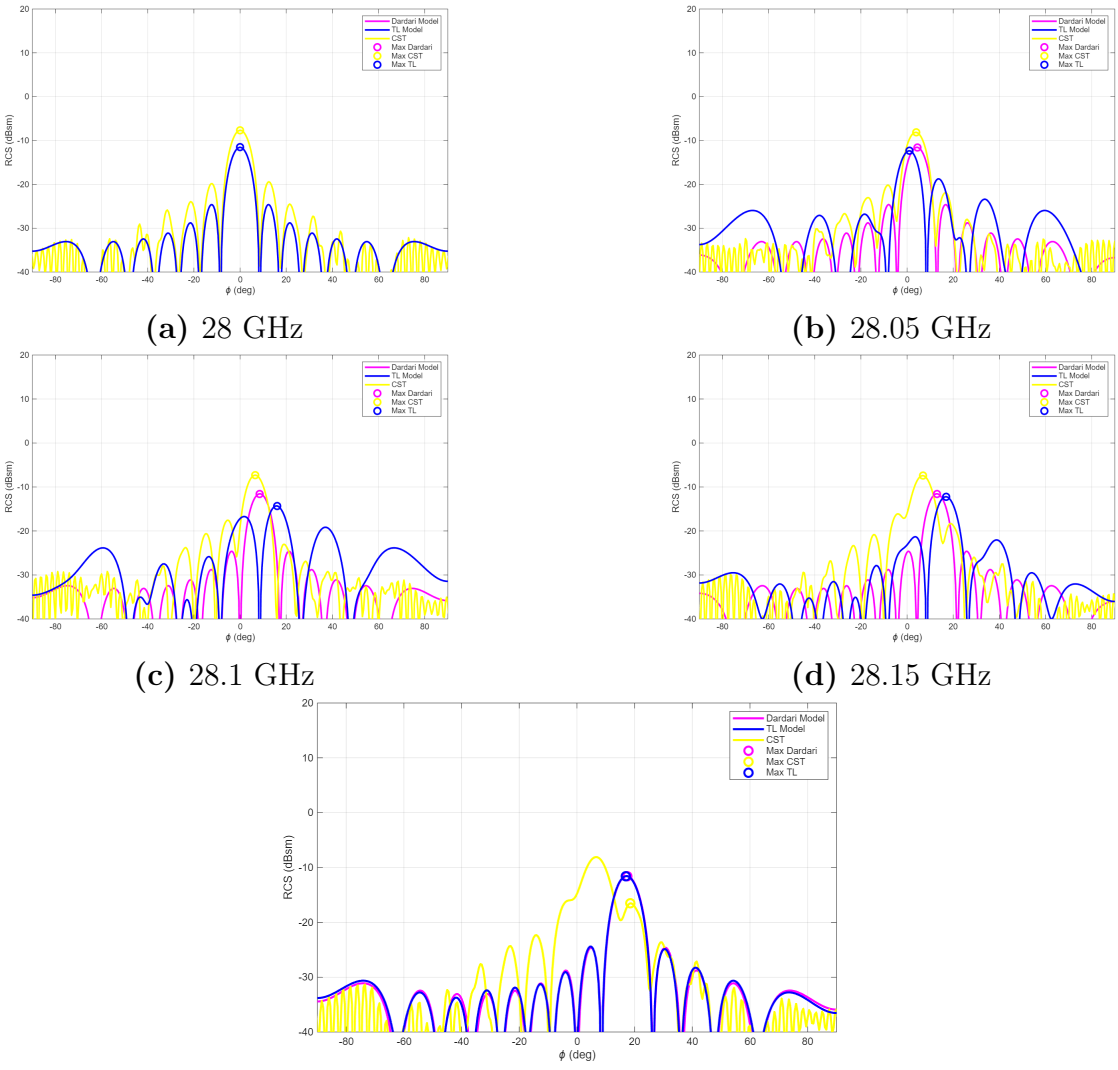

(a) 28 GHz

(b) 28.05 GHz

(c) 28.1 GHz

(d) 28.15 GHz

(e) 28.2 GHz

Figure 3.11: Bistatic RCS of the 12-cell smart skin for different frequencies in the selected bandwidth.

Table 3.7: Main reflection angle obtained by the three models for the 12-cell configuration.

Frequency [GHz]	Ideal Model	TL Model	CST Simulation
28.00	0	0	0
28.05	4.5	2.5	4
28.10	8.5	16	6.5
28.15	13	17	7
28.20	17.5	17	18.5

The analysis of the radiation patterns reveals a clear improvement with respect to the 7-cell configuration. As the operating frequency increases from 28 GHz, the main reflection lobe gradually shifts away from the specular direction, indicating that the metasurface successfully converts frequency variations into angular deviations of the reflected beam. In particular, the CST simulations show that the reflection angle evolves in an approximately linear manner up to about 28.1 GHz. This behavior closely follows the trend predicted by the ideal metaprism model and indicates that the finer spatial sampling of the phase gradient effectively improves the beam steering mechanism. Beyond this frequency, however, the evolution of the reflected beam becomes less regular. The angular displacement of the reflection lobe begins to deviate from the expected trajectory, indicating that the effective phase gradient imposed by the metasurface no longer follows the ideal linear trend. This deviation suggests that dispersive effects associated with the waveguide cavities start to influence the phase response of the metasurface elements.

3.3.4 Phase Gradient Analysis

To further understand the observed beam steering behavior, the spatial phase distribution along the metasurface aperture is analyzed. Figure 3.12 shows the phase delay distribution obtained from the ideal model, the transmission line approximation and the CST full-wave simulations.

The CST phase profiles show a smoother spatial evolution compared to the 7-cell configuration. The phase gradient remains approximately linear for frequencies close to the design frequency, which explains the nearly linear beam steering behavior observed in the RCS analysis. However, at higher frequencies the phase distribution progressively deviates from the ideal linear

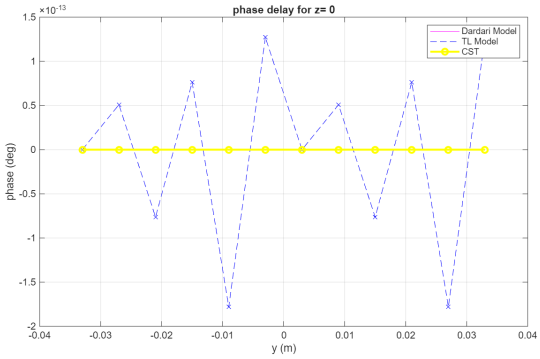

(a) 28 GHz

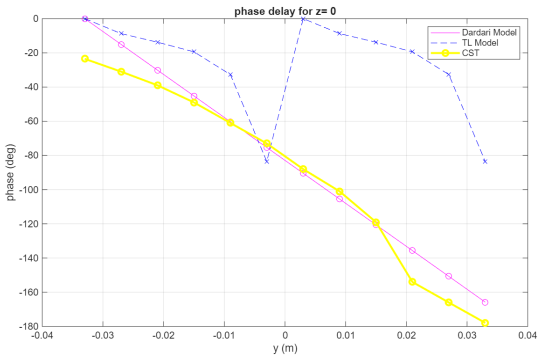

(b) 28.05 GHz

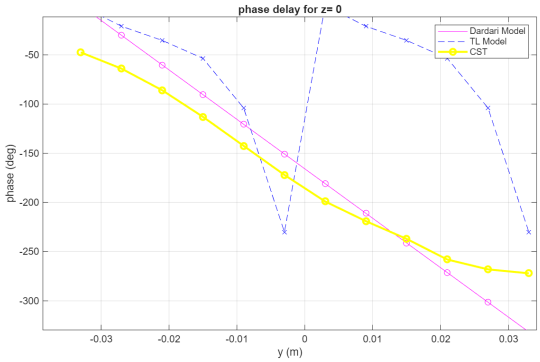

(c) 28.1 GHz

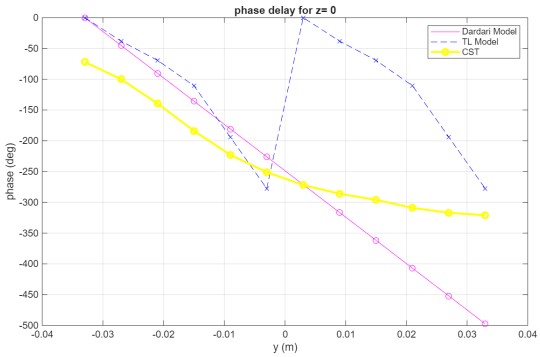

(d) 28.15 GHz

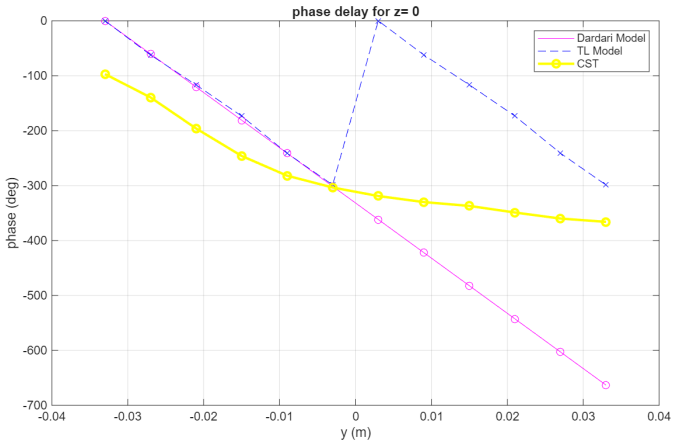

(e) 28.2 GHz

Figure 3.12: Spatial phase delay along the 12-cell metasurface.

trend. These distortions introduce small variations in the effective phase gradient and lead to the deviation of the reflection angle observed beyond approximately 28.1 GHz.

3.3.5 Discussion

The 12-cell configuration represents a clear improvement with respect to the 7-cell metasurface. The finer spatial sampling of the phase gradient allows the reflected beam to evolve more smoothly as the operating frequency varies. In particular, the CST simulations reveal an approximately linear beam steering behavior between 28 GHz and 28.1 GHz, indicating that the metasurface successfully reproduces the fundamental metaprism mechanism within this frequency range. However, the angular evolution begins to deviate from the ideal linear trend at higher frequencies, suggesting that the dispersive phase response of the waveguide cavities gradually influences the effective phase gradient. These results indicate that increasing the number of cells improves the spatial approximation of the ideal phase distribution, but the overall behavior of the metasurface remains partially limited by the electromagnetic properties of the unit-cell structure. A further increase in the number of elements is therefore investigated in the following sections.

3.4 14-Cell Smart Skin

3.4.1 Motivation for Increasing the Number of Cells

In order to better evaluate how the increase of unit cell could affect the spatial approximation of the phase distribution the number of unit cell was increased to 14, to observe the impact of few new unit cells. A larger number of elements allows the phase gradient to be sampled more finely along the metasurface aperture, reducing the phase difference between adjacent cells and providing a closer approximation of the continuous phase distribution assumed in the analytical metaprism formulation [5].

This refinement is expected to produce a smoother angular evolution of the reflected beam as the operating frequency varies.

The purpose of this section is therefore to evaluate how the increase in the number of cells affects the frequency behavior of the metasurface.

3.4.2 Array Geometry

The 14-cell metasurface is obtained by extending the phase gradient implemented in the 7-cell configuration while maintaining the same unit-cell design and periodicity p.

The resulting aperture length becomes

$$L = 14p \tag{3.16}$$

which corresponds to a doubling of the physical aperture with respect to the baseline configuration.

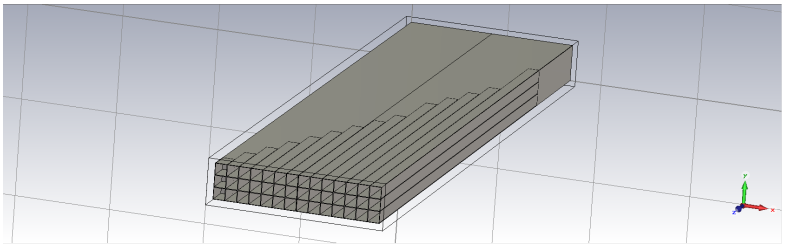

Figure 3.13: CST model of the 14-cell Smart Skin metasurface.

The larger aperture improves the angular resolution of the reflected radiation pattern and reduces the relative influence of edge diffraction effects. At the same time, the increased number of cells enables a finer spatial sampling of the phase gradient across the metasurface.

3.4.3 Phase Sampling Strategy

The phase distribution of the 14-cell array is obtained from the phase response of the unit cell described in the previous section.

Each cavity height is selected in order to reproduce the required phase progression across the metasurface aperture. Compared to the 7-cell configuration, the larger number of elements allows the phase cycle to be distributed over a greater number of cells, resulting in a smaller phase difference between adjacent elements.

Table 3.8 reports the selected cavity heights used in the CST implementation and Figure 3.14 displays the corresponding phase for each considered lengths.

Table 3.8: Selected cavity heights for the 14-cell metasurface.

Cell Index	Height h [mm]
1	12.06
2	27.74
3	43.429
4	59.112
5	74.795
6	90.48
7	106.16
8	121.85
9	137.53
10	168.89
11	184.577
12	200.26
13	215.82
14	262.99

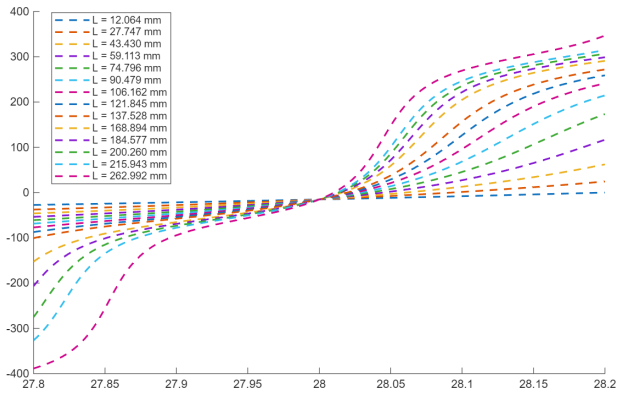

Figure 3.14: Phase response of the selected lengths

Compared to the 7-cell case, the phase difference between adjacent elements is significantly reduced, which improves the approximation of the desired linear phase gradient.

In contrast, the 14-cell configuration provides a more gradual variation of the effective phase gradient along the surface as shown in figure 3.14. As a result, the reflected beam exhibits a more continuous angular displacement when the frequency changes.

Nevertheless, the angular evolution observed in the CST simulations does not perfectly follow the ideal linear trend predicted by the analytical metaprism model. The deviation from linearity becomes visible at higher frequencies, where the reflection angle slightly diverges from the theoretical prediction.

This discrepancy indicates that the practical metasurface does not impose an exactly linear phase gradient across the aperture, mainly due to the dispersive phase response of the waveguide cavities.

3.4.4 Frequency Evolution of the Reflection Pattern

To evaluate the frequency-dependent behavior of the metasurface, the RCS pattern is computed at several frequencies within the considered band.

Figure 3.15 illustrate the evolution of the radiation pattern between 28 GHz and 28.2 GHz.

Table 3.9: Main reflection angle obtained by the three models for the 14-cell configuration.

Frequency [GHz]	Ideal Model	TL Model	CST Simulation
28.00	0	0	0
28.05	4.5	14.5	4.5
28.10	8.5	14.5	6
28.15	13	14.5	16.5
28.20	17.5	16	16.5

A more detailed analysis of the frequency evolution highlights an important improvement with respect to the 7-cell configuration.

In the ideal metaprism model derived from [5], the angular position of the reflected beam varies linearly with frequency. This behavior originates from the linear relationship between the imposed phase delay and the operating frequency, which results in a constant spatial phase gradient across the surface.

As a consequence, the reflection lobe progressively shifts away from the specular direction as the frequency increases.

The analytical transmission line model reproduces a similar qualitative behavior. However, due to the dispersive nature of the guided propagation inside the metallic cavities, the resulting phase gradient does not perfectly

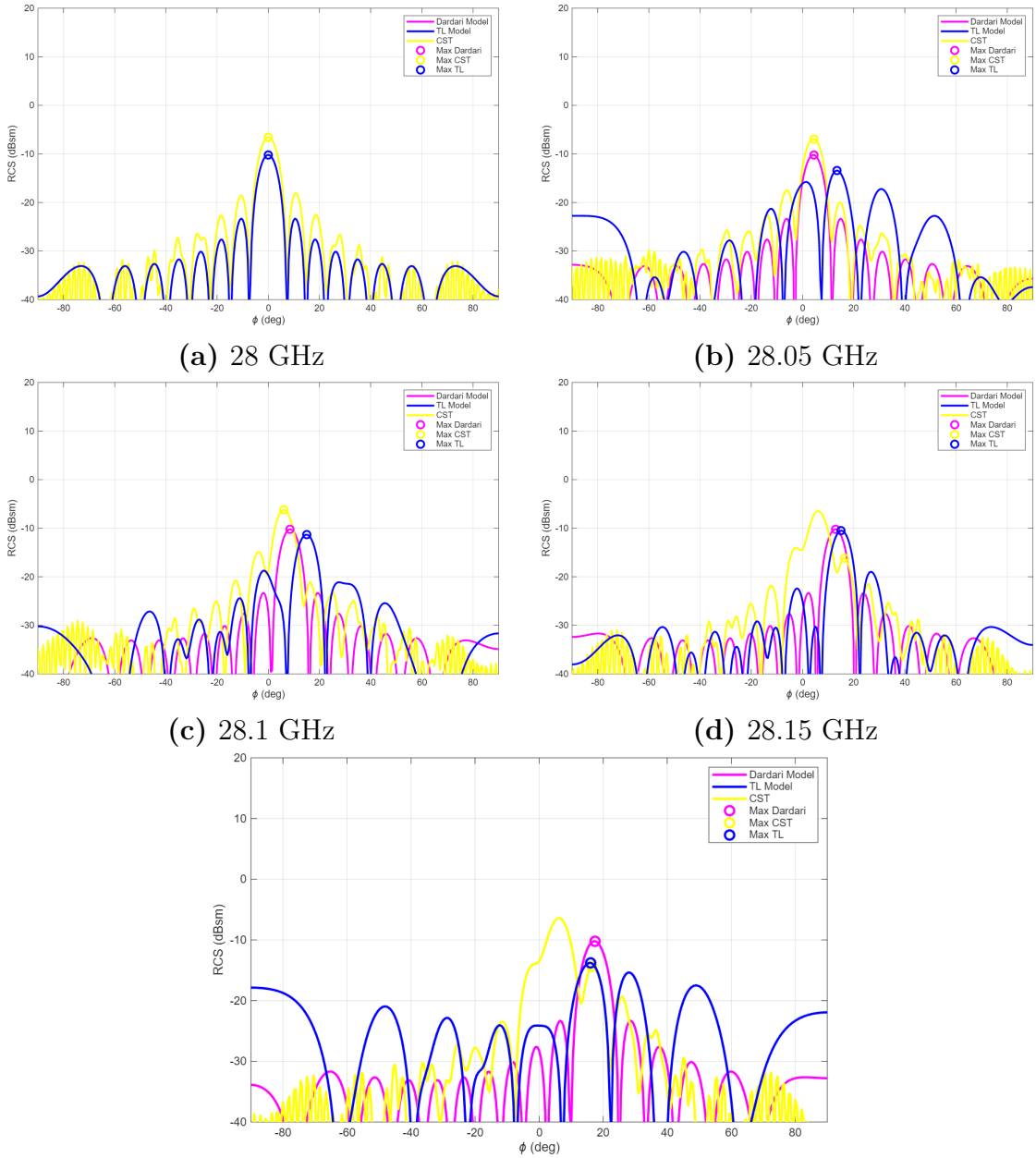

(a) 28 GHz **(b)** 28.05 GHz

(c) 28.1 GHz **(d)** 28.15 GHz

(e) 28.2 GHz

Figure 3.15: Bistatic RCS of the 14-cell smart skin for different frequencies in the selected bandwidth.

follow the ideal linear law predicted by the metaprism formulation.

The full-wave CST simulations provide further insight into the physical

implementation of the metasurface.

Unlike the 7-cell configuration, where the reflection lobe exhibited an abrupt transition between the specular and anomalous directions, the 14-cell metasurface shows a significantly smoother angular evolution as shown in the 12-cell case, leading to an understanding of the behavior around this number of unit cells. In particular, the CST results reveal that the position of the main reflection lobe evolves approximately linearly as the frequency increases from 28 GHz to 28.1 GHz, creating a trend in around this number of unit cells.

Although the angular values do not perfectly coincide with the ideal prediction, the important aspect is that the beam displacement follows a continuous trend.

For instance, at 28.1 GHz the ideal metaprism model predicts a reflection angle of approximately 8.5°, while the CST simulation exhibits a reflection lobe around 6°. This difference indicates that the effective phase gradient implemented by the physical metasurface is slightly smaller than the ideal one.

Nevertheless, the linear evolution of the reflection angle demonstrates that the metasurface successfully reproduces the fundamental metaprism mechanism, where frequency variations are converted into controlled angular deviations of the reflected beam.

This behavior confirms that increasing the number of cells improves the spatial sampling of the phase gradient and enables a more accurate approximation of the ideal metaprism operation.

3.4.5 Phase Gradient Analysis

To further investigate the beam steering behavior observed in the RCS analysis, the spatial phase distribution along the metasurface is examined. According to the metaprism formulation, anomalous reflection is produced by imposing a spatial phase gradient across the surface. In the ideal case, this gradient follows a linear profile, corresponding to a constant phase increment between adjacent cells. In practical implementations, however, the phase response of the unit cells is frequency dependent and dispersive. As a consequence, the effective phase distribution along the metasurface may deviate from the ideal linear profile, which directly affects the direction of the reflected beam. Figure 3.16 shows the spatial phase delay along the 14-cell metasurface for different operating frequencies. The comparison is performed

between the ideal analytical model, the transmission line approximation, and the CST full-wave simulations.

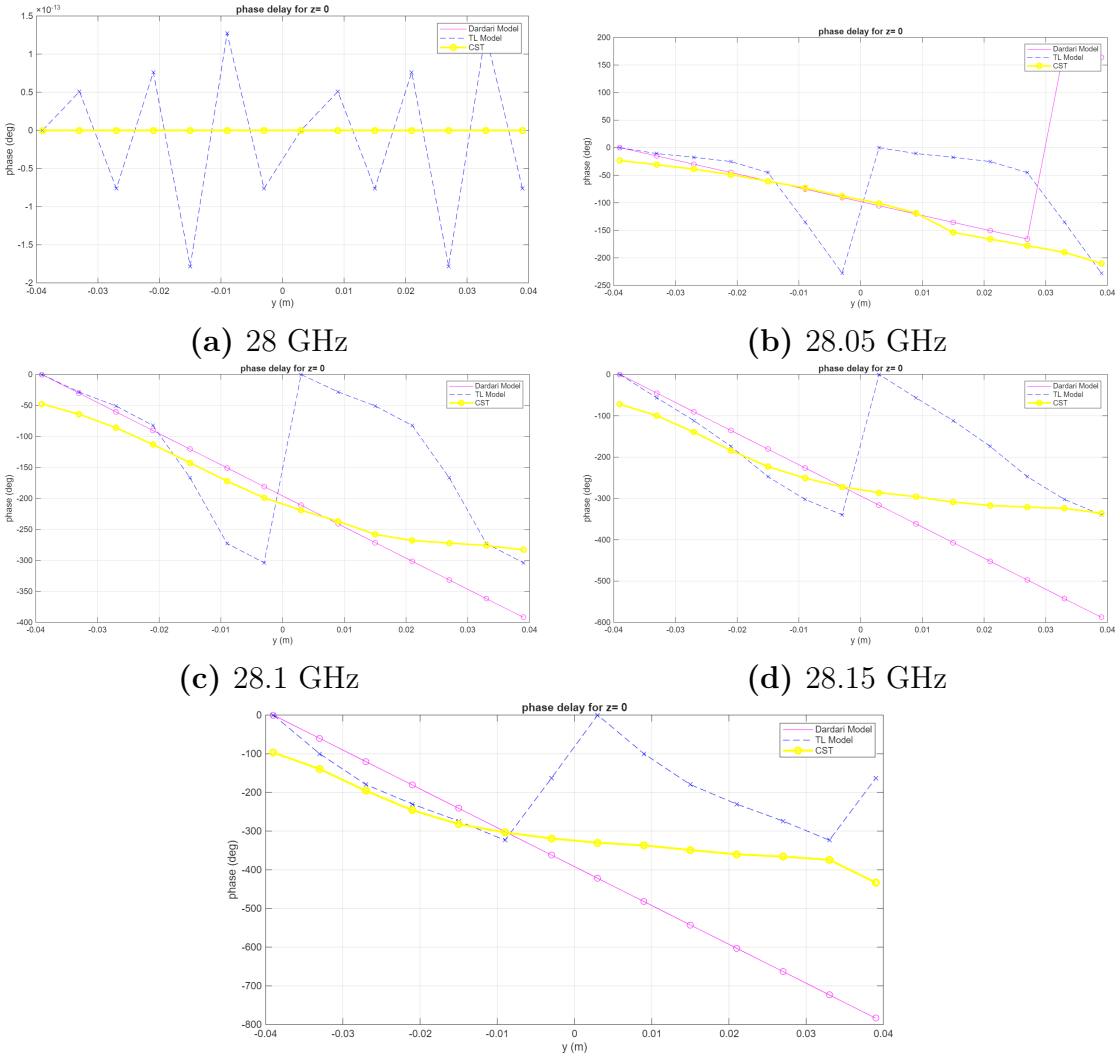

(a) 28 GHz **(b)** 28.05 GHz

(c) 28.1 GHz **(d)** 28.15 GHz

(e) 28.2 GHz

Figure 3.16: Spatial phase delay along the 14-cell metasurface for different frequencies.

The ideal metaprism model exhibits a perfectly linear phase distribution along the surface, which corresponds to the constant phase gradient required to produce controlled beam steering.

The transmission line model partially reproduces this behavior but shows visible discontinuities in the phase profile. These abrupt variations originate

from the dispersive propagation inside the cavities and from the simplified assumptions used in the transmission line approximation.

The CST simulations instead show a phase profile that is generally closer to the ideal linear trend, although small deviations are still present. In particular, the phase gradient remains approximately linear in the central region of the array, while slight distortions appear toward the edges of the metasurface.

These deviations indicate that the effective phase increment between adjacent elements are not perfectly constant along the surface. This effect can be attributed to the dispersive phase response of the waveguide cavities and to electromagnetic coupling between neighboring cells.

As a result, the implemented phase gradient differs slightly from the ideal one, which explains the small discrepancy observed between the predicted and simulated reflection angles in the RCS analysis.

Nevertheless, the overall phase evolution remains sufficiently smooth to produce the approximately linear beam steering behavior observed between 28 GHz and 28.1 GHz. This confirms that increasing the number of cells improves the spatial sampling of the phase gradient and allows the metasurface to better approximate the continuous phase distribution assumed in the ideal metaprism model.

3.4.6 Discussion

The 14-cell metasurface demonstrates a clear improvement with respect to the 7-cell configuration. The finer spatial sampling of the phase gradient allows the reflected beam to evolve more smoothly as the operating frequency varies.

In particular, the CST simulations show an approximately linear beam steering behavior up to about 28.1 GHz, which represents a significant improvement compared to the abrupt transitions observed in the 7-cell case.

Nevertheless, the reflection angles obtained from the full-wave simulations remain smaller than those predicted by the ideal analytical model.

This discrepancy suggests that additional electromagnetic effects, such as cavity dispersion and mutual coupling between adjacent elements, influence the effective phase gradient implemented by the physical metasurface.

To further investigate the role of spatial sampling, the number of cells is increased once more in the next section, leading to the 24-cell configuration.

3.4.7 Transition Toward Higher-Resolution Metasurfaces

Although the 14-cell configuration significantly improves the frequency stability of the reflected beam, further refinement of the spatial sampling can still enhance the metasurface performance.

For this reason, the number of cells is further increased in the following section, leading to a 24-cell and 28-cell configurations. This design aims at approaching even more closely the continuous phase gradient assumed in the ideal metaprism model.

3.5 24-Cell Smart Skin

3.5.1 Motivation for Increasing the Number of Cells

The results obtained for the 6-cell and 12-cell metasurface configurations highlighted the role of spatial sampling in the practical implementation of a metaprism-based Smart Skin.

In the 6-cell configuration, the limited number of elements produced a coarse discretization of the phase gradient, which resulted in an unstable beam steering behavior and the coexistence of specular and anomalous reflection components.

Increasing the number of elements to 12 cells significantly improved the metasurface performance. The finer sampling of the phase distribution allowed a more regular evolution of the reflected beam with frequency, which remained approximately linear up to about 28.1 GHz.

In order to further improve the spatial resolution of the phase gradient, a metasurface composed of 24 unit cells is investigated. From a theoretical perspective, distributing the same 2π phase cycle across a larger number of elements should allow the metasurface to better approximate the continuous phase gradient assumed in the ideal metaprism model.

However, the larger number of elements also requires the use of cavities with larger physical lengths in order to cover the entire phase range.

3.5.2 Array Geometry

The 24-cell metasurface is obtained by extending the same unit-cell geometry used in the previous configurations while maintaining the same periodicity p.

The total aperture length therefore becomes

$$L = 24p \tag{3.17}$$

which corresponds to twice the size of the 12-cell configuration.

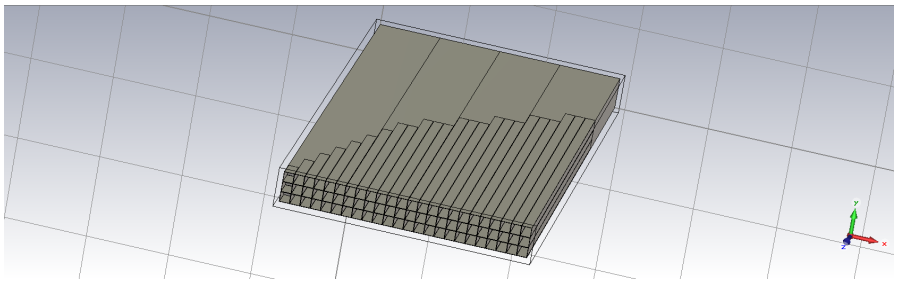

Figure 3.17: CST model of the 24-cell Smart Skin metasurface.

The larger aperture theoretically enables a narrower reflection lobe due to the increased effective size of the metasurface. Moreover, the increased number of elements provides a finer spatial discretization of the phase gradient along the surface.

3.5.3 Phase Sampling Strategy

The phase distribution of the 24–cell metasurface is derived from the phase response of the unit cell presented earlier.

The cavity heights are selected in order to reproduce the required phase progression across the metasurface aperture while covering the entire 2π phase range.

From a geometrical perspective, distributing the phase cycle over 24 elements significantly reduces the phase difference between adjacent cells. This results in a very fine spatial sampling of the phase gradient and should theoretically allow a closer approximation of the continuous phase distribution assumed in the ideal metaprism model. Figure **??** shows the phase response corresponding to the selected cavity lengths.

However, the increase in the number of elements requires the use of cavities with larger physical lengths in order to span the full phase range.

For these larger lengths, the phase response of the waveguide cavities becomes strongly dispersive. As a consequence, the effective phase increments between adjacent elements are not perfectly uniform.

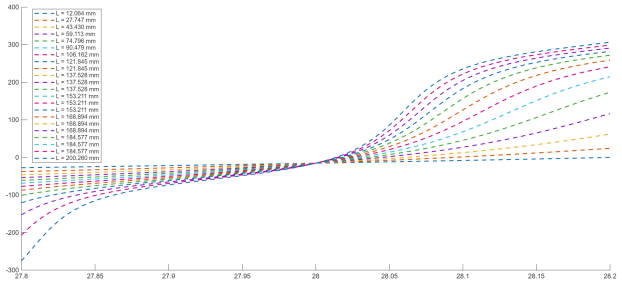

Figure 3.18: Phase response of the selected lengths

This effect distorts the phase gradient implemented along the metasurface, limiting the expected improvement in beam steering performance despite the higher spatial resolution of the array.

3.5.4 Frequency Evolution of the Reflection Pattern

To evaluate the beam steering capability of the metasurface, the bistatic RCS pattern is analyzed for several frequencies within the operating bandwidth.

The figures show that the reflected beam exhibits a limited angular displacement as the frequency increases.

Although an anomalous reflection component appears for higher frequencies, the displacement of the reflection lobe remains relatively small and does not follow the linear evolution predicted by the ideal metaprism model.

Compared to the 12-cell configuration, the increase in the number of cells does not lead to a significant improvement in beam steering performance. To quantify the metasurface behavior, the angular position of the main reflection lobe is extracted from the radiation patterns and compared with the predictions of the analytical models.

Table 3.10: Main reflection angle obtained by the different models for the 24-cell metasurface.

Frequency [GHz]	Ideal Model	TL Model	CST Simulation
28.00	0	0	0
28.05	4.5	0	0.5
28.10	8.5	17	2.5
28.15	13	17	2.5
28.20	17.5	17	4

The CST results show that the reflection angles remain smaller than those predicted by the ideal model, indicating that the effective phase gradient implemented by the physical structure is weaker than the theoretical one.

3.5.5 Phase Gradient Analysis

The spatial phase distribution along the metasurface is analyzed in order to evaluate the effective phase gradient implemented by the structure.

Figure 3.20 shows the phase delay along the metasurface aperture for several operating frequencies, comparing the ideal model, the transmission line approximation and the CST full-wave simulation.

The ideal metaprism model maintains a perfectly linear phase profile along the metasurface, corresponding to a constant phase gradient.

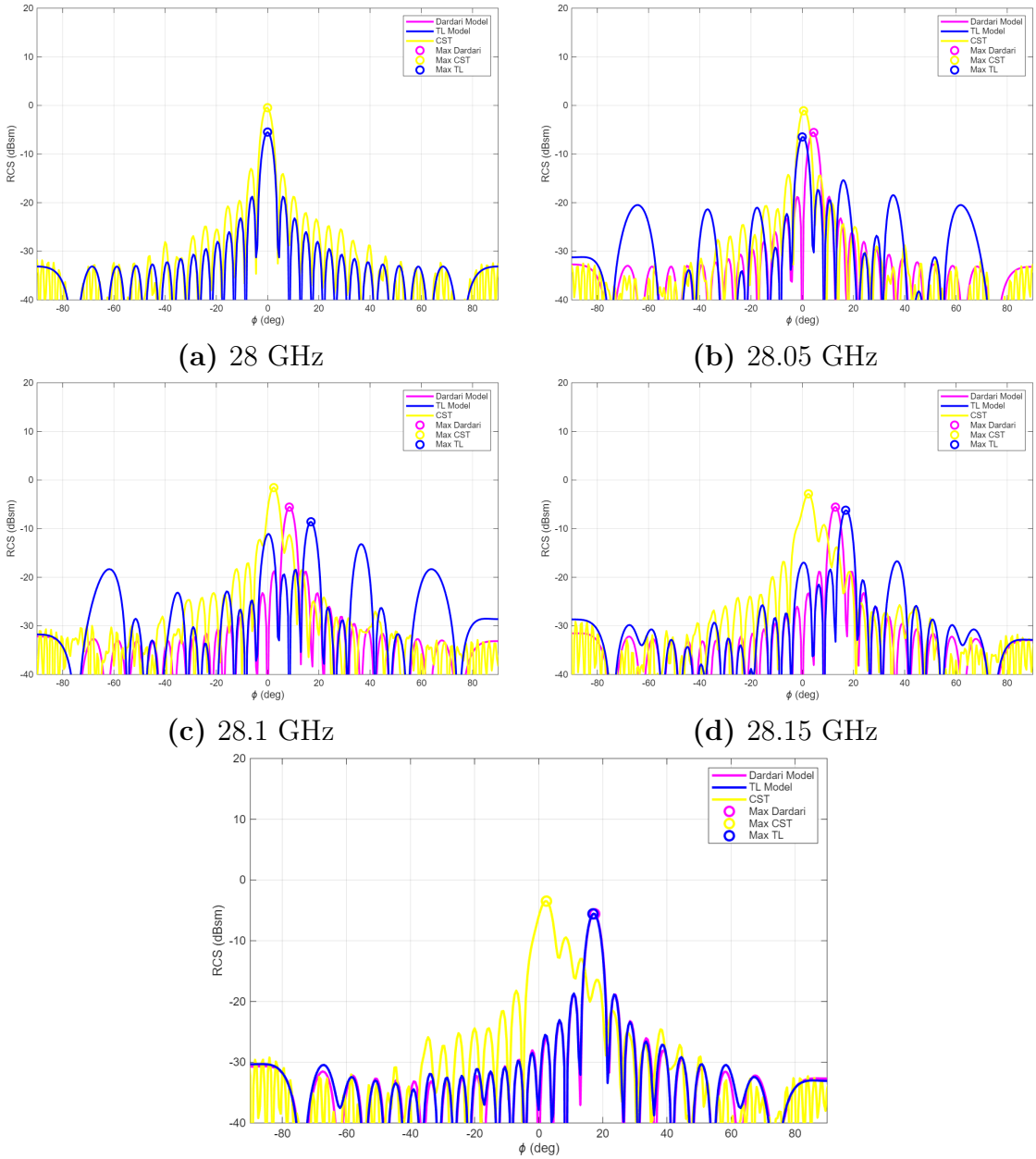

(a) 28 GHz **(b)** 28.05 GHz

(c) 28.1 GHz **(d)** 28.15 GHz

(e) 28.2 GHz

Figure 3.19: Bistatic RCS of the 24-cell smart skin for different operating frequencies.

Both the transmission line model and the CST simulations follow a similar overall trend. However, the CST results reveal that the phase increments

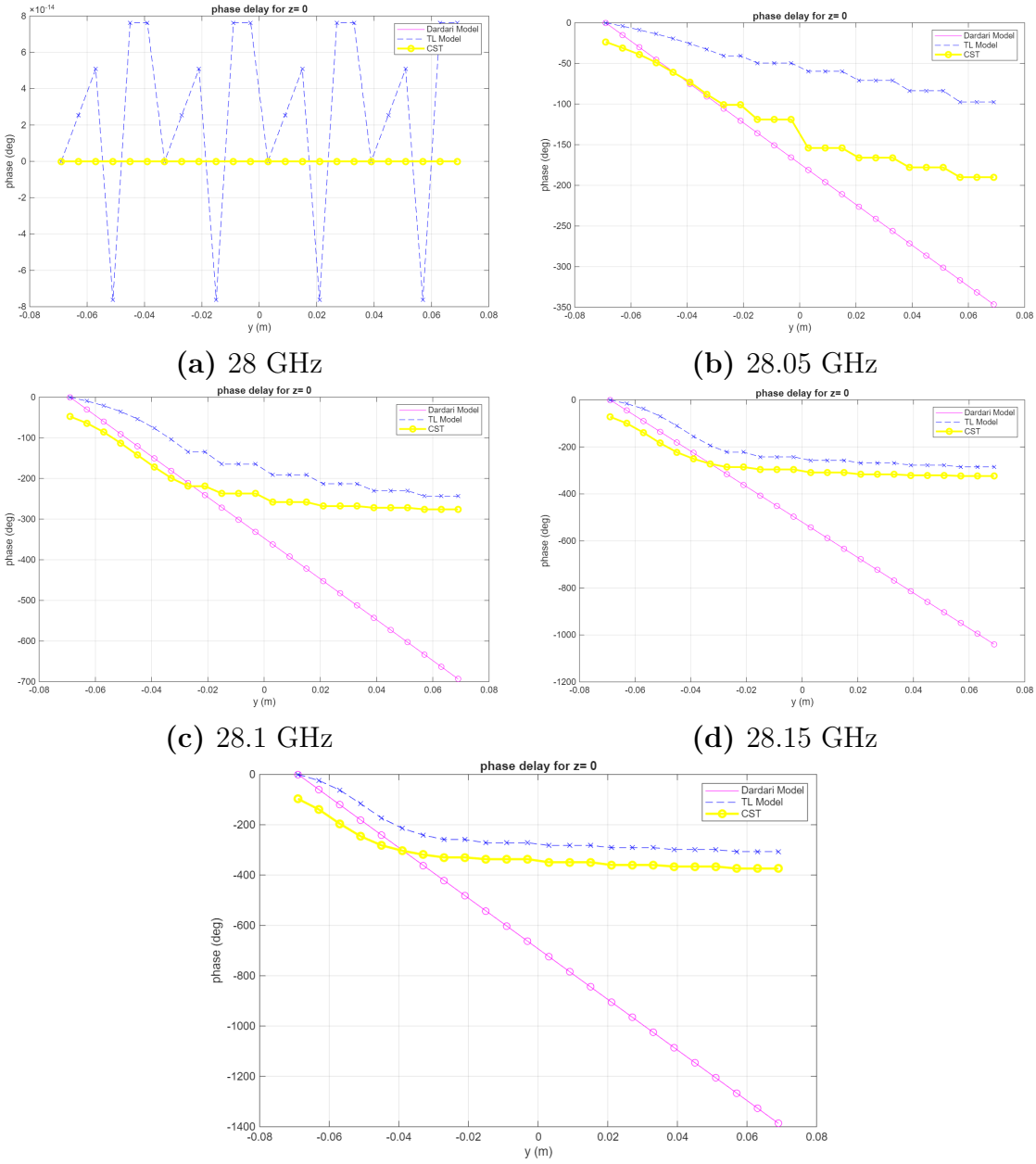

(a) 28 GHz **(b)** 28.05 GHz

(c) 28.1 GHz **(d)** 28.15 GHz

(e) 28.2 GHz

Figure 3.20: Spatial phase delay along the 24-cell metasurface for different frequencies.

between adjacent cells are not perfectly uniform.

These deviations distort the effective phase gradient implemented by the

metasurface, limiting the beam steering capability of the structure.

3.5.6 Discussion

The results obtained for the 24-cell configuration provide important insight into the limitations of the metasurface implementation.

While increasing the number of cells from 6 to 12 produced a noticeable improvement in beam steering behavior, the further increase to 24 cells does not result in a comparable enhancement.

Although the spatial discretization of the phase gradient becomes finer, the angular evolution of the reflected beam remains limited and does not follow the linear trend predicted by the ideal metaprism formulation.

This observation suggests that the metasurface performance is no longer determined only by the spatial sampling of the phase gradient. Instead, the intrinsic electromagnetic response of the unit cells begins to play a dominant role in determining the overall behavior of the structure.

This limitation becomes more apparent when the number of elements is further increased, as shown in the 28-cell configuration analyzed in the following section.

3.6 28-Cell Smart Skin

3.6.1 Motivation for Increasing the Number of Cells

The analysis of the 7-cell and 14-cell configurations demonstrated the importance of the spatial sampling of the phase gradient in the practical implementation of a metaprism-based Smart Skin.

Increasing the number of elements from 7 to 14 cells significantly improved the stability of the reflected beam. The finer sampling of the phase distribution enabled a smoother angular evolution of the reflection lobe and a behavior closer to the frequency-dependent steering predicted by the ideal metaprism model.

However, the CST simulations still revealed a noticeable discrepancy between the reflection angles predicted by the analytical model and those obtained from the full-wave simulations.

In order to further investigate the influence of spatial phase sampling, the metasurface is refined by increasing the number of unit cells to 28. Distributing the same 2π phase cycle across a larger number of elements reduces the phase difference between adjacent cells and theoretically allows a closer approximation of the continuous phase gradient assumed in the metaprism formulation introduced in [5].

From a purely geometrical perspective, this refinement is expected to improve the accuracy of the phase distribution and therefore produce a more regular frequency-dependent beam steering behavior.

3.6.2 Array Geometry

The 28-cell metasurface is obtained by extending the phase gradient implemented in the previous configurations while maintaining the same unit-cell geometry and periodicity p.

The resulting aperture length becomes

$$L = 28p \tag{3.18}$$

which corresponds to four times the size of the original 7-cell configuration.

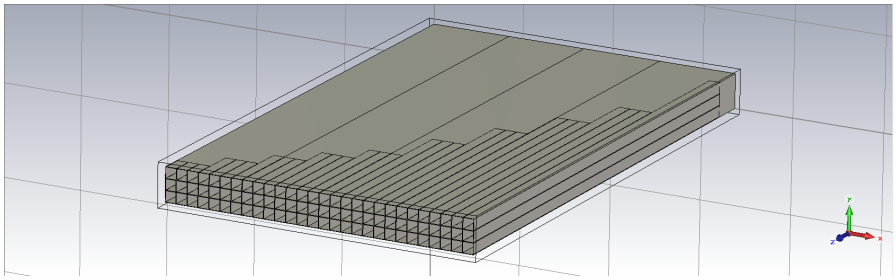

Figure 3.21: CST model of the 28-cell Smart Skin metasurface.

The larger aperture produces a narrower radiation lobe in the reflected field due to the increased effective aperture of the metasurface. Furthermore, the higher number of cells allows the phase gradient to be sampled more finely along the structure, reducing phase quantization effects between adjacent elements.

3.6.3 Phase Sampling Strategy

The phase distribution of the 28–cell metasurface is obtained from the phase response of the unit cell by selecting cavity heights that reproduce the desired phase progression across the metasurface aperture.

With 28 elements, the 2π phase cycle is distributed over a large number of cells, resulting in very small phase differences between adjacent elements. From a purely geometrical perspective, this configuration provides the finest spatial sampling of the phase gradient among all the analyzed metasurfaces. Figure 3.22 illustrates the phase response corresponding to the selected cavity

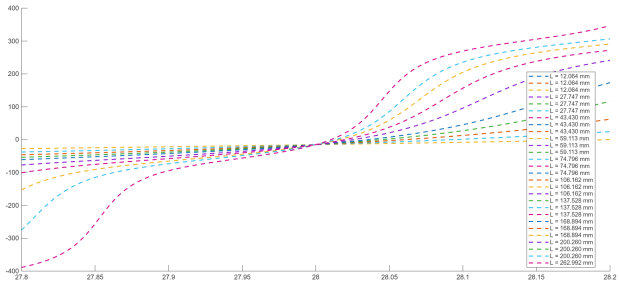

Figure 3.22: Phase response of the selected lengths

lengths.

However, implementing the required phase distribution requires cavities with significantly larger heights compared to the smaller arrays.

For these large cavity lengths, the phase response of the waveguide structure exhibits a strongly nonlinear behavior that resembles a tangent-like curve. In this regime, small frequency variations can produce large phase changes, while other frequency intervals show very limited phase variation.

As a consequence, the phase increments between adjacent cells are no longer uniform and the effective phase gradient imposed along the metasurface deviates from the ideal linear profile.

This phenomenon explains why increasing the number of elements from 14 to 28 does not lead to a proportional improvement in beam steering performance, even though the spatial sampling of the phase gradient becomes significantly finer.

3.6.4 Frequency Evolution of the Reflection Pattern

To analyze the beam steering behavior of the metasurface, the bistatic RCS pattern is evaluated at several frequencies within the operating band.

Figure 3.23 illustrates the evolution of the radiation pattern between 28 GHz and 28.2 GHz.

The figures show how the position of the main reflection lobe evolves as the operating frequency increases.

At low frequencies, the reflected beam remains close to the specular direction. As the frequency increases, the anomalous reflection lobe gradually appears and shifts away from the specular direction.

However, the angular displacement remains relatively small and significantly lower than the values predicted by the ideal metaprism model.

3.6.5 Reflection Angle Comparison

To better quantify the metasurface behavior, the angular position of the main reflection lobe is extracted from the radiation patterns and compared with the predictions of the analytical models.

Table 3.11: Main reflection angle obtained by the different models for the 28-cell metasurface.

Frequency [GHz]	Ideal Model	TL Model	CST Simulation
28.00	0	0	0
28.05	4.5	1	1
28.10	8.5	3	2.5
28.15	13	4	3
28.20	17.5	4	3

The comparison shows that the CST results partially follow the trend predicted by the analytical models. However, the reflection angles remain significantly smaller than those predicted by the ideal metaprism model.

3.6.6 Analysis of the Beam Steering Behavior

The ideal metaprism model predicts a linear relationship between the reflection angle and the operating frequency. This behavior originates from the constant spatial phase gradient imposed across the metasurface.

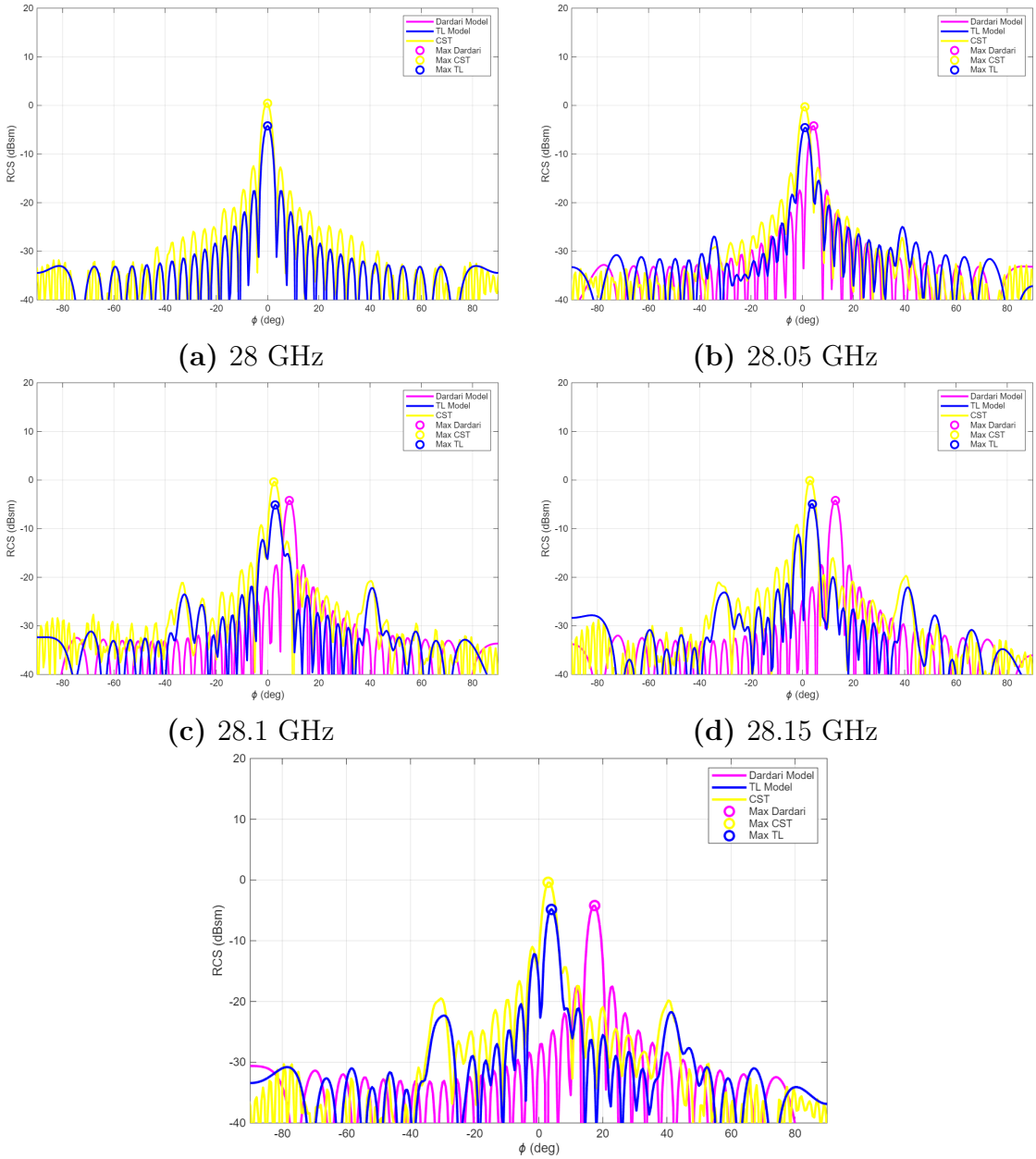

(a) 28 GHz **(b)** 28.05 GHz

(c) 28.1 GHz **(d)** 28.15 GHz

(e) 28.2 GHz

Figure 3.23: Bistatic RCS of the 28-cell smart skin for different frequencies in the selected bandwidth.

The CST simulations show the initial appearance of this linear trend. However, as the frequency increases, the observed behavior progressively

approaches that predicted by the transmission line (TL) model.

In particular, the reflection angles obtained from the CST simulations remain smaller than the theoretical values predicted by the ideal model. This indicates that the effective phase gradient implemented by the physical structure is slightly weaker than the ideal one.

This discrepancy can be attributed to several electromagnetic effects that are not fully captured by the simplified analytical models. Among the most relevant factors are the dispersive phase response of the waveguide cavities, the mutual coupling between adjacent elements, and diffraction phenomena associated with the finite size of the metasurface.

Influence of the Waveguide Phase Response A deeper understanding of the behavior observed in the 28–cell configuration can be obtained by analyzing the intrinsic phase response of the waveguide cavities used as unit cells.

The phase delay introduced by each element is obtained through the propagation of the electromagnetic field inside a metallic waveguide cavity operating close to its cutoff frequency. In this regime, the phase response of the cavity is strongly dispersive and depends nonlinearly on the cavity length.

Figure 3.24 illustrates the evolution of the reflection phase as a function of frequency for several cavity lengths.

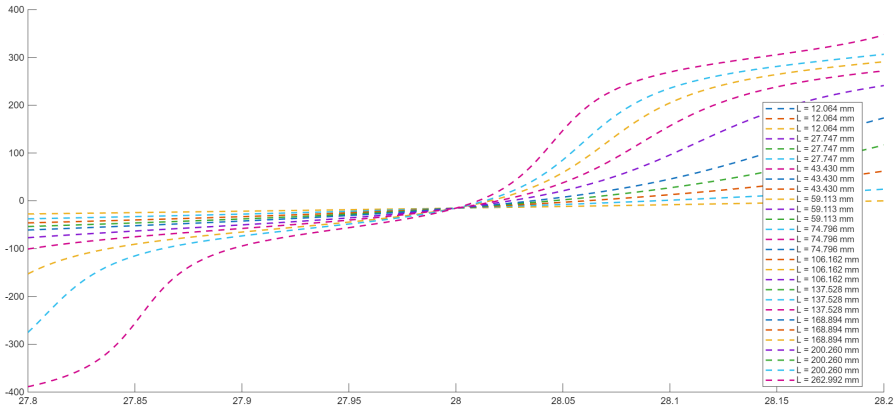

Figure 3.24: Reflection phase as a function of frequency for different cavity lengths.

For relatively small cavity lengths, the phase variation can be locally approximated as quasi–linear within the considered frequency range. However,

as the cavity height increases, the phase response progressively deviates from linearity and begins to resemble a tangent-like behavior.

This effect becomes particularly evident for the largest cavity lengths required to synthesize the phase distribution of the 28–cell metasurface.

As a consequence, the phase increments between adjacent cells are no longer uniform, and the spatial phase gradient imposed along the metasurface deviates from the ideal linear profile assumed in the metaprism formulation.

This phenomenon explains why the 28–cell configuration does not provide a significant improvement compared to the 14–cell case. Although the spatial sampling of the metasurface is increased, the electromagnetic response of the individual cavities becomes the dominant limiting factor.

In contrast, in the 12–cell and 14–cell configurations the required cavity lengths remain within a region where the phase response is still approximately linear. For this reason, the metasurface is able to reproduce the expected beam steering behavior more accurately in those cases.

3.6.7 Phase Gradient Analysis

The spatial phase distribution along the metasurface is also analyzed for the 28-cell configuration in order to evaluate the effect of further increasing the spatial resolution of the phase gradient.

Figure 3.25 shows the phase delay along the metasurface aperture for different operating frequencies, comparing the ideal model, the transmission line approximation, and the CST full-wave simulation.

The ideal metaprism model maintains a perfectly linear phase profile across the entire aperture, corresponding to a constant spatial phase gradient.

Both the transmission line model and the CST simulations follow a similar overall trend, confirming that the larger number of cells allows a finer spatial sampling of the phase distribution.

However, the CST results show noticeable deviations from the ideal linear profile. In particular, the phase gradient becomes progressively distorted along the metasurface, indicating that the effective phase increment between adjacent cells is not perfectly uniform. Instead, the phase distribution tends to follow a behavior similar to that predicted by the TL model.

These deviations can be attributed to the dispersive phase response of the waveguide cavities and to the electromagnetic coupling between neighboring elements.

As a consequence, the improvement obtained by increasing the number of

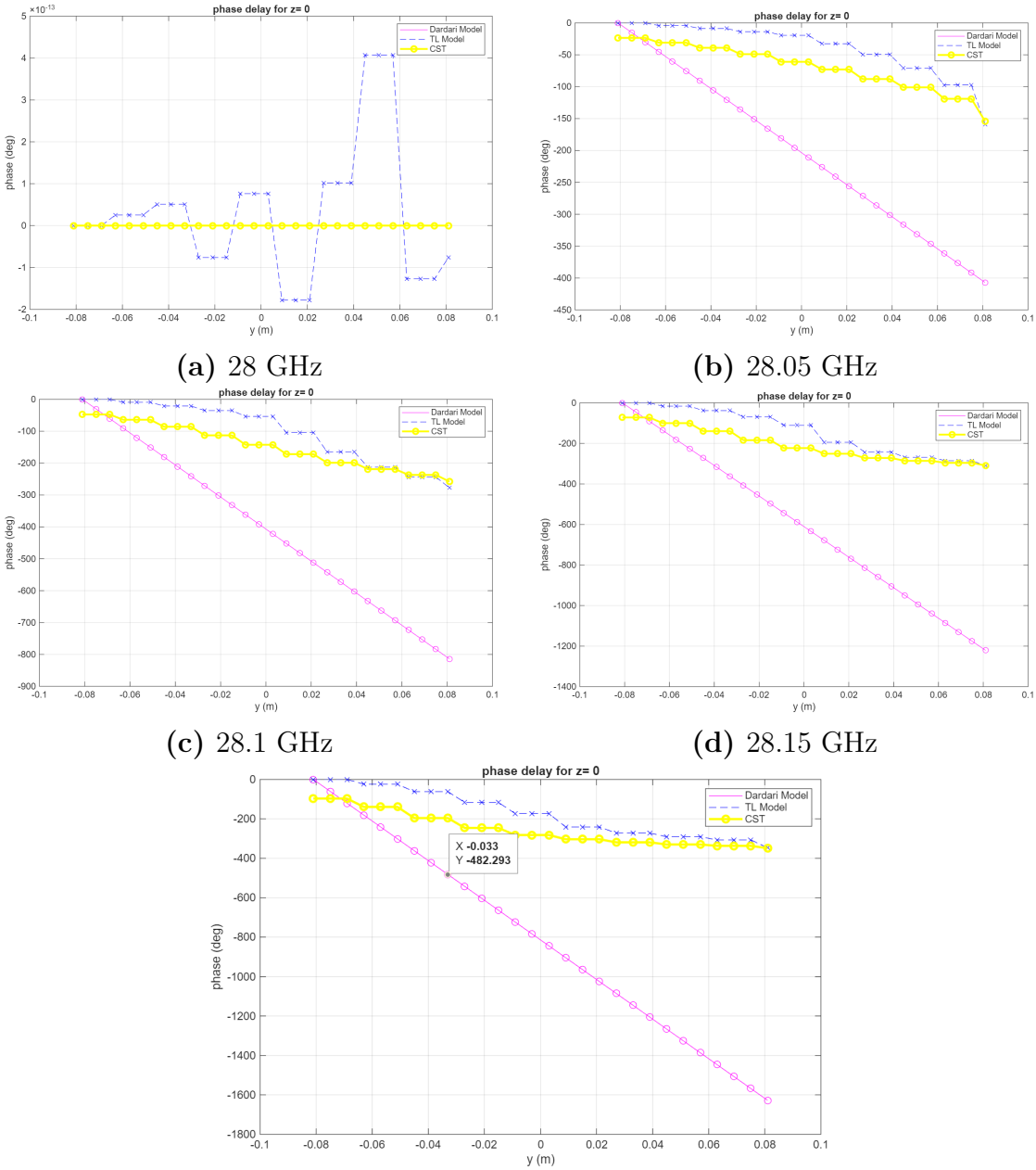

(a) 28 GHz

(b) 28.05 GHz

(c) 28.1 GHz

(d) 28.15 GHz

(e) 28.2 GHz

Figure 3.25: Spatial phase delay along the 28-cell metasurface for different frequencies.

cells from 14 to 28 is limited. While the spatial phase distribution becomes smoother, the overall beam steering behavior remains similar to that observed

in the 14-cell configuration.

This observation suggests that once the phase gradient is sampled with sufficient spatial resolution, other electromagnetic effects become the dominant factors influencing the metasurface performance. Therefore, simply increasing the number of unit cells does not necessarily lead to a further improvement in the linearity of the beam steering behavior.

3.6.8 Discussion

The results obtained for the 28-cell configuration provide useful insight into the role of spatial sampling in metaprism metasurfaces.

Increasing the number of elements from 7 to 14 produced a significant improvement in the stability of the beam steering behavior. However, the further increase from 14 to 28 cells does not lead to a proportional improvement.

Although the reflection lobe exhibits a slightly smoother evolution, the overall angular behavior remains comparable to that observed in the 14-cell configuration.

This observation indicates that the metasurface performance is no longer primarily limited by the discretization of the phase gradient. Instead, other electromagnetic effects begin to dominate the response of the structure.

Consequently, further improvements in metaprism performance may require not only increasing the number of elements, but also optimizing the unit-cell design and the phase tuning mechanism in order to better control the dispersive behavior of the waveguide cavities.

Chapter 4

Conclusions

This thesis investigated the design and electromagnetic behavior of a Smart Electromagnetic Skin operating at 28 GHz, with the objective of evaluating its capability to manipulate electromagnetic waves for future wireless communication systems.

The work was developed within the framework of Smart Radio Environments, where the propagation channel is no longer considered a passive medium but can be actively controlled through engineered electromagnetic surfaces. In this context, metasurfaces and Smart Skins represent promising solutions to enhance signal coverage and enable advanced wavefront manipulation techniques.

The study focused on the implementation of a metaprism-based reflective metasurface capable of producing frequency-dependent beam steering through a controlled spatial phase gradient. Starting from the theoretical metaprism model, a practical implementation based on metallic waveguide cavities was designed and analyzed through full-wave electromagnetic simulations.

The unit cell was first characterized in order to determine the relationship between cavity height and reflection phase. By properly selecting the cavity dimensions, a phase response covering the entire 2π range was obtained, enabling the synthesis of the phase gradient required for anomalous reflection.

Several metasurface configurations were then investigated in order to evaluate the influence of the spatial sampling of the phase gradient. Six structures composed of 6, 7, 12, 14, 24 and 28 unit cells were designed and simulated.

The results showed that the metasurface performance strongly depends on the number of elements used to implement the phase gradient. The 6-cell and

7-cell configurations exhibited a coarse discretization of the phase distribution, which produced unstable beam steering behavior and the coexistence of specular and anomalous reflection components.

A significant improvement was obtained with the 12-cell and 14-cell configurations. In these cases, the finer spatial sampling of the phase gradient allowed the metasurface to reproduce a smoother phase distribution along the aperture. As a consequence, the reflected beam exhibited a more regular angular evolution with frequency, showing an approximately linear behavior up to about 28.1 GHz. These configurations therefore represent the most effective trade-off between spatial sampling and electromagnetic response of the unit cells.

Further increasing the number of elements to 24 and 28 cells did not lead to additional improvements. Although the spatial resolution of the phase gradient becomes finer, the required cavity lengths increase significantly, and the phase response of the waveguide structures becomes strongly dispersive. In this regime the phase response tends to follow a tangent-like behavior, which distorts the phase gradient across the metasurface and limits the achievable beam steering performance.

As a result, the larger metasurface configurations do not provide a better agreement with the ideal metaprism model, and in some cases the angular evolution of the reflected beam becomes less regular.

Overall, the results demonstrate that the proposed metasurface is capable of implementing the fundamental metaprism mechanism, converting frequency variations into controlled angular deviations of the reflected beam. At the same time, the study highlights the importance of considering the intrinsic electromagnetic behavior of the unit cells when designing practical metasurface implementations.

4.1 Future Perspectives

Future research could focus on improving the phase response of the unit cell in order to reduce the dispersive behavior observed for large cavity lengths. Alternative geometries or different resonant structures may allow a more linear phase variation over the operating bandwidth.

Another possible direction involves the optimization of the phase distribution across the metasurface by using numerical optimization techniques that take into account the actual electromagnetic response of the unit cells.

Finally, the integration of tunable or reconfigurable elements could enable dynamic control of the phase gradient, allowing the realization of programmable Smart Skins capable of adapting their electromagnetic response in real time.

Such developments could further enhance the potential of metasurface-based technologies for future millimeter-wave communication systems.

Bibliography

[1] Marco Di Renzo, Alessio Zappone, Merouane Debbah, Mohamed-Slim Alouini, Chau Yuen, Julien de Rosny, and Sergei Tretyakov. *Smart Radio Environments Empowered by Reconfigurable Intelligent Surfaces: How it Works, State of Research, and Road Ahead*. 2020. arXiv: 2004.09352 [cs.IT]. URL: https://arxiv.org/abs/2004.09352 (cit. on pp. 1, 2, 4, 7, 8).

[2] Walid Saad, Mehdi Bennis, and Mingzhe Chen. *A Vision of 6G Wireless Systems: Applications, Trends, Technologies, and Open Research Problems*. 2019. arXiv: 1902.10265 [cs.IT]. URL: https://arxiv.org/abs/1902.10265 (cit. on p. 2).

[3] Christopher Holloway, Edward Kuester, Josh Gordon, John O'Hara, Jim Booth, and D. Smith. «An Overview of the Theory and Applications of Metasurfaces: The Two-Dimensional Equivalents of Metamaterials». In: *Antennas and Propagation Magazine, IEEE* 54 (Apr. 2012), pp. 10–35. DOI: 10.1109/MAP.2012.6230714 (cit. on pp. 2, 7).

[4] Qingqing Wu and Rui Zhang. «Towards Smart and Reconfigurable Environment: Intelligent Reflecting Surface Aided Wireless Network». In: *IEEE Communications Magazine* 58.1 (2019), pp. 106–112. DOI: 10.1109/MCOM.001.1900107 (cit. on p. 4).

[5] Davide Dardari and Devis Massari. *Using MetaPrisms for Performance Improvement in Wireless Communications*. 2020. arXiv: 2003.13505 [eess.SP]. URL: https://arxiv.org/abs/2003.13505 (cit. on pp. 6, 9, 10, 26, 27, 39, 49, 52, 64).

[6] Nanfang Yu and Federico Capasso. *Flat optics with designer metasurfaces*. Feb. 2014. DOI: 10.1038/nmat3839 (cit. on pp. 6, 7, 13).

[7] B. A. Munk. *Frequency Selective Surfaces*. New York: John Wiley & Sons, 2000 (cit. on p. 7).

[8] Kebin Fan, Jonathan Y. Suen, Xinyu Liu, and Willie J. Padilla. «All-dielectric metasurface absorbers for uncooled terahertz imaging». In: *Optica* 4.6 (June 2017), pp. 601–604. DOI: 10.1364/OPTICA.4.000601. URL: https://opg.optica.org/optica/abstract.cfm?URI=optica-4-6-601 (cit. on p. 8).

[9] Xin Su et al. *Reconfigurable Intelligent Surfaces: Standardization Oriented Analysis and Considerations*. 2024. DOI: 10.1109/MCOMSTD.0001.2400034 (cit. on p. 8).

[10] Muhammad Zain Siddiqi and Talha Mir. «Reconfigurable intelligent surface-aided wireless communications: An overview». In: *Intelligent and Converged Networks* 3.1 (2022), pp. 33–63. DOI: 10.23919/ICN.2022.0007 (cit. on p. 8).

[11] Giacomo Oliveri, Francesco Zardi, Giorgio Gottardi, and Andrea Massa. «Optically Transparent Electromagnetic Skins for Millimeter-Wave Wireless Communications». In: *IEEE Access* 12 (2024), pp. xxxx–xxxx. DOI: 10.1109/ACCESS.2024.xxxxxx (cit. on p. 9).

[12] Alvaro F. Vaquero, Eduardo Martinez-de-Rioja, Manuel Arrebola, José Encinar, and Maha Achour. «Smart Electromagnetic Skin to Enhance Near Field Coverage in mm-Wave 5G Indoor Scenarios». In: *IEEE Transactions on Antennas and Propagation* PP (May 2024), pp. 1–1. DOI: 10.1109/TAP.2024.3383216 (cit. on p. 9).

[13] Silvia Palmucci, Andrea Abrardo, Davide Dardari, Alberto Toccafondi, and Marco Di Renzo. «Metaprism Design for Wireless Communications: Angle-Frequency Analysis, Physical Realizability Constraints, and Performance Optimization». In: *arXiv preprint arXiv:2501.06760* (2025) (cit. on p. 9).

[14] Marina Lotti, Giacomo Calesini, and Davide Dardari. «NLOS Localization Exploiting Frequency-Selective Metasurfaces». In: *arXiv preprint arXiv:2307.12800* (2023) (cit. on p. 9).

[15] Davide Tornielli Bellini, Dario Tagliaferri, Marouan Mizmizi, Stefano Tebaldini, and Umberto Spagnolini. «Multi-View Near-Field Imaging in NLOS with Non-Reconfigurable EM Skins». In: (2024), pp. 384–389. DOI: 10.1109/ICCWorkshops59551.2024.10615761 (cit. on p. 9).

[16] A. A. Saharian, L. Sh. Grigoryan, and H. F. Khachatryan. *Radiation processes in dielectric cylindrical waveguides*. 2026. arXiv: 2601.03688 [physics.optics]. URL: https://arxiv.org/abs/2601.03688 (cit. on p. 14).